Romanian Reports in Physics, Vol. 68, Supplement, P. S483–S538, 2016

NUCLEAR RESONANCE FLUORESCENCE EXPERIMENTS AT ELI-NP

C.A. UR[1,a], A. ZILGES[2], N. PIETRALLA[3], J. BELLER[3], B. BOISDEFFRE[1], M.O. CERNĂIANU[1], V. DERYA[2], B. LÖHER[3], C. MATEI[1], G. PASCOVICI[3], C. PETCU[1], C. ROMIG[3], D. SAVRAN[5], G. SULIMAN[1], E. UDUP[1], V. WERNER[3]

[1]ELI-NP, "Horia Hulubei" National Institute for Physics and Nuclear Engineering, 30 Reactorului Street, RO-077125, Bucharest-Magurele, Romania
[2]Institut für Kernphysik, Universität zu Köln, Zülpicher Str. 77, 50937 Köln, Germany
[3]Technische Universität Darmstadt, Schlossgartenstr. 9, 64289 Darmstadt, Germany
[4]ExtreMe Matter Institute, GSI Helmholtzzentrum für Schwerionenforschung GmbH, Planckstr. 1, 64291 Darmstadt, Germany
[a] Corresponding author *E-mail*: calin.ur@eli-np.ro

Abstract. The development at ELI-NP of a new laser-based Inverse Compton Scattering gamma beam system, featuring extremely high intensities at very narrow bandwidths, opens new and important opportunities in nuclear science research. Nuclear photonics is undergoing a revival, the gamma beams with unprecedented features delivered at ELI-NP paving the way for high accuracy and detailed nuclear physics studies. A wide range of industrial, homeland security and healthcare applications will also experience an important boost. The combination of nuclear photonics with the technique of Nuclear Resonance Fluorescence (NRF) allows for the recovery of several physical quantities characterizing the excited nuclear states in a completely model independent way. These observables include the excitation energies, level widths, gamma-decay branching ratios, spin quantum numbers, and parities.

In the last decade, the NRF technique allowed for the discovery and detailed study of various phenomena in atomic nuclei. Examples are the collective magnetic dipole Scissors Mode in deformed nuclei, quadrupole excitations with mixed proton-neutron symmetry, the electric Pygmy Dipole Resonance, octupole coupled excitations, or alpha-cluster states.

The present Technical Design Report (TDR) deals with the application of the NRF technique at ELI-NP to study forefront nuclear structure research topics. The document presents some of the physics cases to be investigated and discusses the feasibility of the proposed experiments. The advanced characteristics of the gamma beams available at ELI-NP and the use of high efficiency detection systems will offer a powerful combination, unique in the world, for the investigation of the proposed physics cases.

The main detection system for the NRF studies is a multi-detector array (**ELIADE** - **ELI**-NP **A**rray of **DE**tectors) based on the use of composite high-purity Ge detectors and large volume $LaBr_3$ scintillator detectors able to detect with high efficiency gamma rays with energies up to several MeV in the presence of the high radiation background produced by the gamma beams. Gamma-ray energies and angular distributions will be measured with high accuracy. The design of the array is made highly flexible to allow for an easy transposition in different locations in the high- and low-energy gamma beam areas, a fast change of configuration based on the needs of the experiments, the use of the detectors in other setups and easy maintenance to reduce the downtimes.

NRF measurements will be possible starting from early stages of the Gamma Beam System operation at ELI-NP with both low- and high-energy gamma beams. Already in the initial phase of operation at low-energies below 3.5 MeV the gamma beams at ELI-NP will be competitive with the present state-of-the-art gamma beam systems.

Key words: Gamma beam system, nuclear resonance fluorescence, gamma-ray spectroscopy, digital data acquisition.

1. INTRODUCTION

1.1. THE TECHNIQUE OF NUCLEAR RESONANCE FLUORESCENCE

Photonuclear reactions below 20 MeV will allow for the study of various nuclear decay modes. Photoinduced nuclear excitations with energies below the particle separation energies will decay exclusively by subsequent re-emission of γ-radiation (see Fig. 1.1 left side). This reaction type is denoted as Nuclear Resonance Fluorescence (NRF) [1–4]. Primary observables of NRF processes are the energies, intensities, polarizations, and angular intensity distributions of the fluorescent γ-radiation.

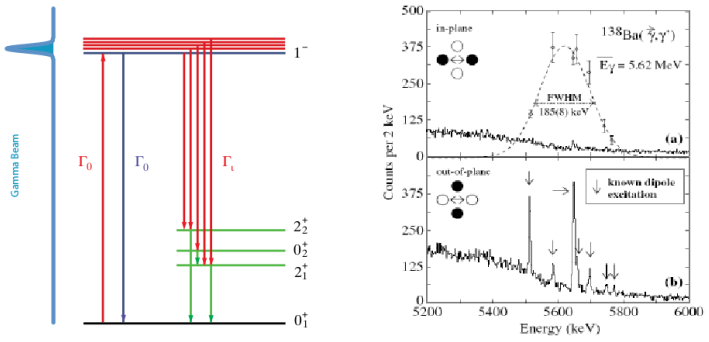

Figure 1 – Schematic illustration of the NRF process starting from a $J^\pi = 0^+$ ground state of a nucleus with an incoming γ beam of small bandwidth [22] (left-hand side). Beam energy distribution and gamma-ray intensity registered with HPGe detectors in-plane and out-of-plane with respect to the beam polarization plane [16] (right hand side)

The cross section for an NRF process on the ground state with total angular momentum J_0 of an unoriented ensemble through an isolated bound nuclear state at excitation energy E_r, with total angular momentum J, and mean lifetime τ leading to a final state with total angular momentum J_f has the Breit-Wigner form:

$$\frac{d^2\sigma}{d\Omega dE} = \pi\lambda\!\!\!^{-2}\frac{g}{2}\frac{\Gamma_0\Gamma_f}{(E-E_r)^2+\Gamma^2/4}\frac{W_{J_0JJ_f}(\Omega)}{4\pi} \qquad (1)$$

with $\lambda\!\!\!^{-} = \hbar c/E_r$ and the "spin-factor" $g = (2J+1)/(2J_0+1)$, $\Gamma = 1/\tau = \sum \Gamma_i$ is the total decay width of the bound resonance, $\Gamma_{0(f)}$ is the partial decay width to the ground (final) state, and $W_{J_0JJ_f}(\Omega)$ denotes the angular distribution function of the scattered photons with respect to the incident beam axis. $W_{J_0JJ_f}(\Omega)$ is determined by the involved angular momentum quantum numbers and by the multipolarities of the initial and final photons. The angular distribution function $W_{J_0JJ_f}(\theta,\phi)$ of the photon scattering reaction is equivalent [3, 4] to a correlation function of a direction-polarization correlation and can be expanded in terms of Legendre polynomials. In the absence of parity violation and third order multipole contributions for the $J_0^{\pi_0}(L_1, L_1') \rightarrow J^{\pi}(L_2, L_2') \rightarrow J_f^{\pi_f}$ cascade, it can be written as:

$$W(\theta,\phi) = \sum_{\nu=0}^{even} B_\nu(\vec{\gamma_1}) A_\nu(\gamma_2) P_\nu \cos\theta + (\pm)_{L_1} \cos 2\phi \sum_{\nu=2}^{even} B'_\nu(\vec{\gamma_1}) A_\nu(\gamma_2) P_\nu^{(2)} \cos\theta \tag{2}$$

where P_ν and $P_\nu^{(2)}$ denote the ordinary and the unnormalized associated Legendre polynomials of order ν. Here, $(\pm)_{L_1}$ takes the value +1 (-1) in case of electric (magnetic) character of the leading multipole L_1 of the first transition. Using the phase convention of Krane, Steffen, and Wheeler [5] for the multipole mixing ratios δ_1 and δ_2 the expansion coefficients A, B, and B' can be written in terms of tabulated F-coefficients [5] as:

$$A_\nu(\gamma_2) = \frac{1}{1+\delta_2^2}[F_\nu(L_2, L_2, J_f, J) + 2\delta_2 F_\nu(L_2, L_2', J_f, J) + \delta_2^2 F_\nu(L_2', L_2', J_f, J)] \tag{3a}$$

$$B_\nu(\vec{\gamma_1}) = \frac{1}{1+\delta_1^2}[F_\nu(L_1, L_1, J_0, J) - 2\delta_1 F_\nu(L_1, L_1', J_0, J) + \delta_1^2 F_\nu(L_1', L_1', J_0, J)] \tag{3b}$$

$$B'_\nu(\vec{\gamma_1}) = \frac{1}{1+\delta_1^2}[\kappa_\nu(L_1, L_1) F_\nu(L_1, L_1, J_0, J) + 2\delta_1 \kappa_\nu(L_1, L_1') F_\nu(L_1, L_1', J_0, J) \tag{3c}$$

$$- \delta_1^2 \kappa_\nu(L_1', L_1') F_\nu(L_1', L_1', J_0, J)]$$

The κ coefficients can be found in Ref. [6].

The partial widths γ_i for electromagnetic decay into the i^{th} decay channel are the sum over all multipoles $\Gamma_i = \sum \Gamma_{i,\pi\lambda}$ with the monopolar partial decay widths being related to the reduced transition rates $B(\pi\lambda; J \rightarrow J_f)$ by:

$$\Gamma_{i,\pi\lambda} = 8\pi \sum_{\pi=\pm,\lambda=1}^{\infty} \frac{\lambda+1}{\lambda[(2\lambda+1)!!]^2} \left(\frac{E_\gamma}{\hbar c}\right)^{2\lambda+1} B(\pi\lambda; J \rightarrow J_f) \tag{4}$$

The reduced transition rates B are proportional to the squares of the electromagnetic transition matrix elements from the initial to the final nuclear quantum state. They carry information about the structure of the nuclear wave functions involved. That information can be directly compared to the results of nuclear structure models without having introduced any model-dependence in its determination. This feature makes NRF measurements very valuable sources of information on nuclear structure.

To summarize again, the comprehensive list of physical quantities that can be determined either directly or indirectly in NRF experiments includes:

- γ-ray transition energies
- level energies
- angular momentum quantum numbers
- parity quantum numbers
- resonant photon scattering cross sections
- level lifetimes and total decay widths
- γ-decay branching ratios
- K-quantum numbers
- transition multipolarities and multipole mixing ratios
- partial decay widths
- reduced transition rates $B(E1)$, $B(M1)$, or $B(E2)$.

1.2. HISTORY AND STATUS OF THE FIELD

First NRF experiments were reported by Moon *et al.* [7] who managed to compensate for the energy loss due to the nuclear recoil by using a Doppler up-shift of the γ-ray energies in mounting the γ-ray source on a high-speed centrifuge. In 1958 the process of NRF received a great deal of attention when Goldhaber *et al.* [8] managed to establish the negative helicity of the neutrino in an artful experiment with γ-rays from the weak decay of the radioisotope ^{152}Eu. In the same year Mössbauer [9] discovered the phenomenon of recoilless γ-ray emission and subsequent resonance absorption. Mössbauer spectroscopy established a new method for research with unprecedented accuracy for the details of atomic hyperfine interactions and many applications in atomic or molecular physics, chemistry, geology, biology, material sciences, and fundamental physics.

Continuous-energy photon beams such as bremsstrahlung overcame the problem of recoil-energy detuning. Schiff initially proposed [10] the use of bremsstrahlung for nuclear reactions in 1946. A decade later Hayward and Fuller managed to first observe NRF induced by a bremsstrahlung beam [11]. With the advent of high-current, high-duty factor electron accelerators intense sources of bremsstrahlung became available for photonuclear reactions. In the energy range that we discuss here, NRF studies, photofission and photoactivation experiments were performed at several bremsstrahlung sites worldwide. An early review article was published already in 1959 by Metzger [1]. In the 1980s the NRF activities intensified by the discovery of the low-energy M1 nuclear scissors mode by Richter and his group at Darmstadt [12]. Later on, the status of the field has repeatedly been updated by review articles of Kneissl and collaborators [2–4].

It has always been the wish of researchers to have a tunable quasi-monochromatic source for γ-rays in the MeV range. Attempts were made in the 1960s by positron annihilation-in-flight [13] and tagged photons [14]. However, these sources lacked either in intensity or in monochromaticity. In the 1990s tunable quasi-monochromatic γ-ray sources were developed on the basis of elastic scattering of intense photon beams from high-intensity lasers on highly-relativistic electron beams in head-on collisions. These Laser Compton Backscattering (LCB) processes provide currently the most brilliant sources of photons in the γ-ray energy regime for which the parameters like energy, bandwidth, time structure or polarization are controllable by the experimentalists. A proof-of-principle demonstration of NRF studies at LCB photon beams was done by Ohgaki *et al.* in 1994 [15]. The method of NRF at LCB photon beams finally matured into a superior method for nuclear structure discoveries [16–19] when instrumental progress of LCB beams were realized at the High Intensity γ-ray Source (HIγS) [20, 21] at the Duke Free Electron Laser Laboratory (DFELL).

Since the initial NRF experiments at HIγS in 2001 [16–18] nuclear structure studies by NRF represented one of the main pillars of the photonuclear program at the HIγS facility. Very recently, a significant break-through was made by Löher *et al.* [22] when demonstrating the successful operation of a γ-γ-coincidence spectroscopy set-up at the LCB photon beam at HIγS. The combination of an intense mono-energetic photon beam, which defines the excitation energy, with γ-γ coincidence spectroscopy of the following decays offers ideal conditions to investigate in detail the decay behavior of photo-excited states. The experiences and scientific results gained over the last ten years (e.g. [19, 22–28]) clearly demonstrate the great scientific potential of an NRF experimental site at a next-generation LCB source at ELI-NP.

The determination of parities of dipole-excited states in even-even nuclei is straight-forward using a polarized gamma-ray beam and a polarimeter setup. Using

detector pairs at 90° with respect to the beam axis, horizontal and vertical to the plane spanned by the beam axis and the polarization vector, one detects γ rays from the ground-state decay of 1^+ or 1^- excited states only in the parallel or vertical detectors, respectively (see Fig. 1 right side). Fig. 2 illustrates the corresponding angular distributions, and for comparison the angular distribution of a $0^+ \rightarrow 2^+ \rightarrow 0^+$ cascade. In case of an E2 excited state, additional detectors at backward angles will allow for an unambiguous determination of the spin.

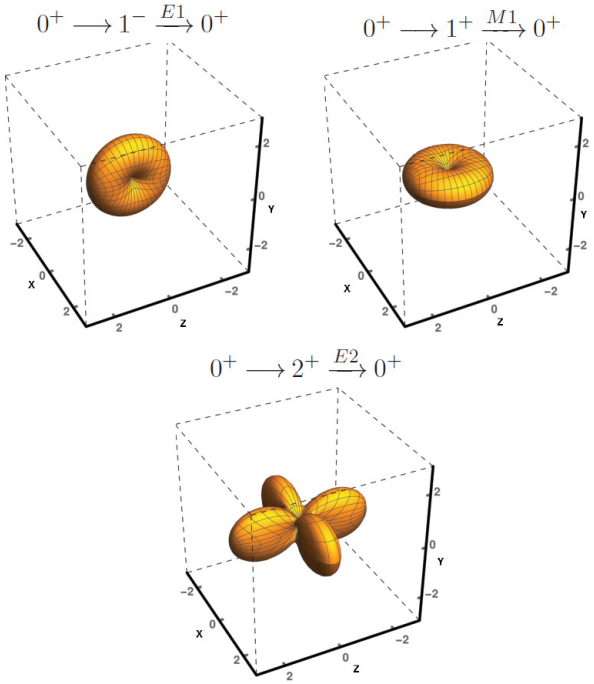

Figure 2 – Angular distributions from the decay to the ground-state of 1^+, 1^-, and 2^+ states excited by a linearly polarized photon beam. The beam axis is along the z axis; the polarization vector is along the x axis.

Based on the number of photons scattered in the horizontal plane (N_H) and the vertical plane (N_V) one can define the asymmetry by the relation:

$$A = Q \times P \times \Sigma = Q \times P \times \frac{N_H - N_V}{N_H + N_V} \tag{5}$$

where Q is the polarisation sensitivity of the polarimeter setup, P is the degree of beam polarisation and Σ is the analyzing power. For ideal polarisation of the incoming beam (P=1), values of $A = 1$ correspond to magnetic dipole excitations, and $A = -1$ to electric dipole excitations. The asymmetry can also be used in order to

determine multipole-mixing ratios of transitions from dipole excited states. This is illustrated in Fig. 3, where the asymmetry is given as a function of the multipole-mixing ratio δ. Comparison to the experimentally obtained asymmetry then gives the possible values of δ.

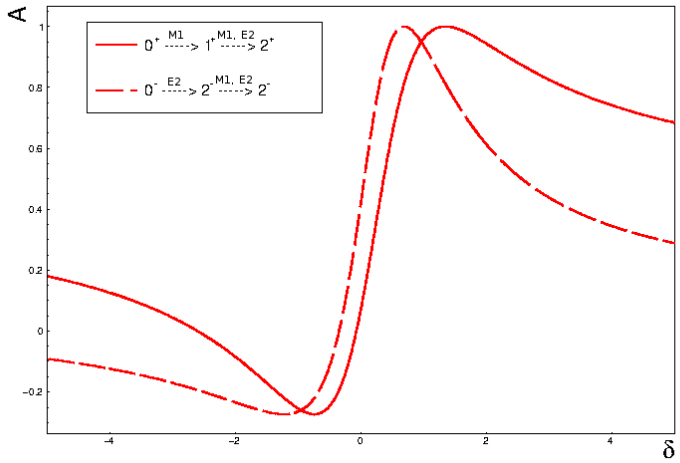

Figure 3 – Analyzing power as a function of the multipole mixing ratio for dipole and quadrupole exited states decay to a lower-lying $J = 2$ state

However, in general the obtained values are not unique. This problem can be overcome by adding detectors at backward angles, where additional differences in the angular distributions of, e.g., E2 or M1 de-excitations occur, as shown for example for a $0^+ \rightarrow 2^+ \rightarrow 2^+$ transition cascade in Fig. 4. Other possible cascades, for example involving a $1^+ \rightarrow 1^-$ transition, also have distinct angular distributions. The ELIADE detector array (see Section 3 for details) will allow for a unique assignment of spins and parities of photo-excited states, as well as of multipole mixing ratios of their decays to lower-lying states.

2. PHYSICS CASES

The superior characteristics of the photon beam make ELI-NP a unique facility to investigate challenging current problems in nuclear physics. These include the structure of the Pygmy Dipole Resonance (PDR) and its relation to the equation of state of nuclear matter, parity violation of the effective nuclear force, constraints on matrix elements relevant for neutrino-less double-beta decays, the breaking of proton-neutron symmetry in nuclei observed via the scissors mode, electric and mag-

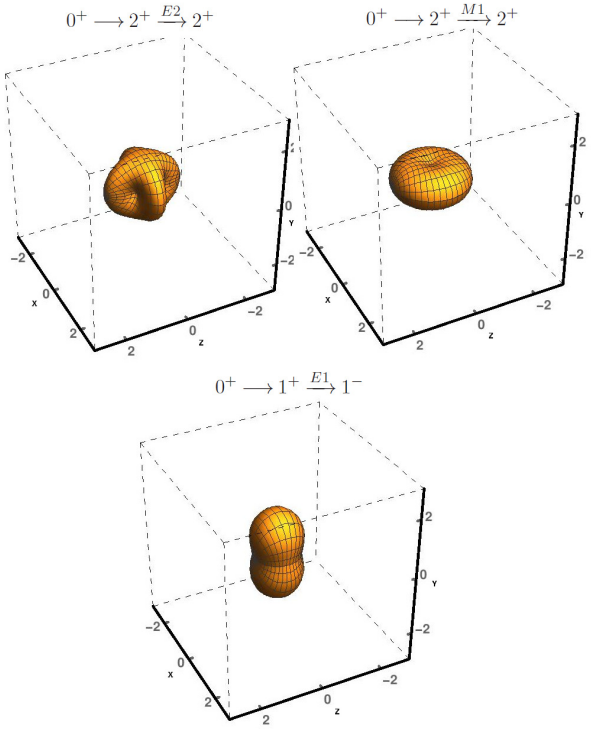

Figure 4 – Angular distributions from $J = 2$ (top) or $J = 1$ (bottom) excited states to lower-lying states assuming given multi-polarities. The beam axis is along the z axis; the polarization vector is along the x axis.

netic dipole moments in actinides, the photo-response of weakly abundant isotopes near shell closure, and the model- and calibration-independent measurement of the widths of bound nuclear excitations. Presented below are examples for experiments addressing these problems. For all cases the principle feasibility with the beam parameters expected for the start version of ELI-NP has been checked, for some critical cases a count rate estimate is provided in Section 4.

2.1. AN ACCESS TO THE EQUATION OF STATE AND TO NEUTRON RICH MATTER: INVESTIGATION OF THE PYGMY DIPOLE RESONANCE

Electric dipole strength in the energy range of about 5-9 MeV is often denoted as Pygmy Dipole Resonance [29]. A common macroscopic interpretation of this strength is as an oscillation of a neutron-skin versus a proton-neutron core. State-of-the-art calculations support that the transition density in the energy region of interest is indeed a surface effect [30] with strong isoscalar components [31]. The PDR then would open a window to the determination of the neutron-skin thickness, and would

potentially have impact on astrophysical scenarios, such as rapid neutron capture rates [32]. The PDR and the complete E1 response of a nucleus can in addition constrain the symmetry energy parameter in the nuclear equation of state [33, 34].

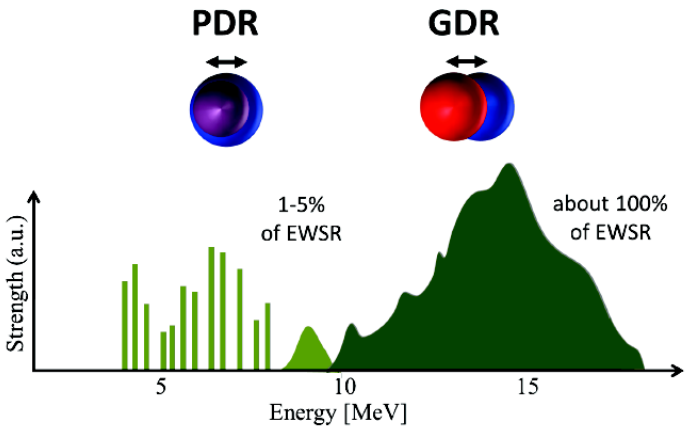

Figure 5 – Schematic distribution of E1 strength in an atomic nucleus showing the splitting into a Pygmy Dipole Resonance (PDR) and a Giant Dipole Resonance (GDR). Octupole-coupled modes which can generate E1 strength at even lower energies are not included.

However, E1 excitation strength due to such an effect would be superimposed on the low-energy tail of the Giant Dipole Resonance (GDR), and present experimental and theoretical efforts aim at identifying a unique fingerprint for a neutron-skin oscillation. In addition, the parameterization of the GDR tail is under debate; therefore, it is of utmost importance to derive proper photon strength functions from data, in order to be able to quantify additional E1 strength on the GDR tail. An important question in this respect is the amount of branching transitions from dipole excited states in the PDR region to lower-lying excited states. Such low energy γ-decay branchings are difficult to observe but they directly re-scale the observed E1 excitation strength. First steps toward γ-coincidence measurements have recently been taken at HIγS within the γ^3 collaboration, and will be applied at the ELI-NP facility, with much enhanced photon fluxes and brilliance - that means that the decay behavior of single or few states at a time can be determined, in addition to separating E1 from M1 (e.g., spin-flip) excitations.

We intend to take data in the PDR energy regions of a variety of isotopes to hitherto unprecedented precision and resolution. This program encompasses spherical nuclei at or near magic shells, as well as investigations into deformed regions. We will focus on specific cases first. The ^{116,124}Sn isotopes offer a test of PDR

in isotopes with very different neutron numbers, and a rich database already exists on which we can base new high-precision measurements. The ^{204,208}Pb nuclei are important isotopes for PDR research since the level density is very low, hence, E1 strength will be concentrated in fewer states allowing for very precise studies. Especially ^{204}Pb with a very ordered low-energy level scheme will allow for a meaningful test of the Axel-Brink hypothesis by coincidence measurements. The Axel-Brink hypothesis states that resonance structures should be built on excited states the same way as on the ground state and is presently the basis of many studies in Nuclear Structure and Nuclear Astrophysics. To probe for changes in the E1 strength distribution as a function of mass number and N/Z ratio, we also intend to investigate ^{140}Ce, ^{90,96}Zr, ^{60}Ni, and ^{52}Cr.

The new data, that is: detailed strength distributions, knowledge on γ-decay branches, and spin and parity information, will serve as a significant database for the derivation of photon strength functions and the validity of assumed level densities. The latter should be even better accessible in deformed nuclei, such as ^{164}Dy or ^{154}Sm, where the level densities at low energies are much higher than in the spherical cases, and statistical calculations involving certain assumptions on level densities, photon strength functions, and branchings can directly be put to a test. In quadrupole deformed nuclei, also a splitting of a PDR, akin to the splitting of the GDR, due to oscillations with respect to the individual symmetry axes can be examined in detail. A first signature of such deformation splitting has recently been observed in pioneering proton scattering experiments on ^{154}Sm at RCNP Osaka [35]. To date, especially in cases of high level densities, excitation strength has to be averaged about rather large energy intervals. At ELI-NP, due to the high brilliance of the beam, selection of either individual excited states, or very narrow averaging bins can be achieved, revealing information on the fine structure of the E1 strength distribution at PDR energies.

2.2. PARITY VIOLATION IN NUCLEAR EXCITATION: THE CASE OF ^{20}NE

Since 1956, when Lee and Yang postulated a mirror-symmetry violation in β-decays [36], and 1957 when Wu experimentally verified the symmetry violation effect [37], parity non-conservation is well known. It has fundamental importance for our understanding of the role of fundamental symmetries in nature. While the electromagnetic force and the strong force conserve parity, the effective nuclear force violates parity due to small contributions of the weak interaction to the effective nucleon-nucleon interaction. Hence, various theoretical and experimental approaches have been used to investigate parity violation in nuclei (details are reviewed in [38, 39]). At the current state of the field, the weak meson-nucleon coupling constants deduced from various experiments are not consistent. Consequently, further investigations of

parity violation in nuclei are desirable.

In particular, the study of parity doublets $J^{\pm}$ is suited to observe parity violation in nuclei. The $J^{\pi} = 1^{+}/1^{-}$ parity doublet in ^{20}Ne at 11.26 MeV excitation energy has been suggested as one of the best cases to study parity violation of isolated nuclear eigenstates [40]. Their excitation energies are reported as 11,258.6(2) keV for the 1^{+} state and $11,255.4(\pm 0.7^{+0.6}_{-1.2})$ keV for the 1^{-} state [41]. The energy difference of the doublet states is only $\Delta E = E(1^{-}) - E(1^{+}) = -(3.2 \pm 0.7^{+1.2}_{-0.6})$ keV [41].

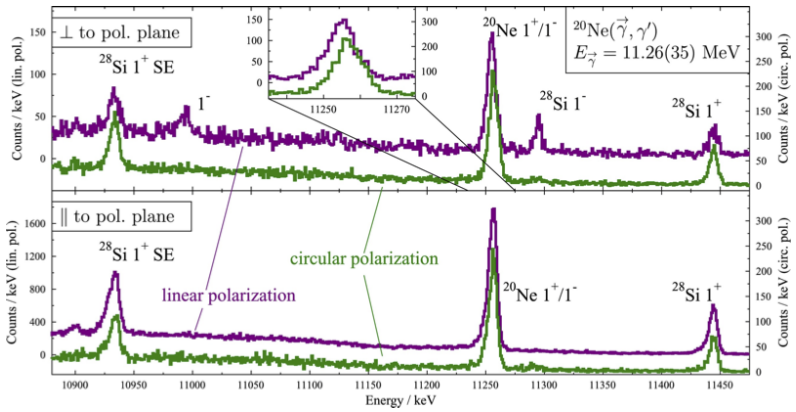

Figure 6 – γ-ray spectra observed perpendicular (upper part) and parallel (lower part) to the polarization plane in the energy region of the parity doublet in ^{20}Ne [41].

The observation of parity violating effects in nuclei is an experimental challenge. In case of the parity doublet of ^{20}Ne a parity violating matrix element $\langle PNC \rangle \equiv |\langle 1^{+}|V_{PNC}|1^{-}\rangle| \approx 1$ eV is expected. Since, an energy splitting of about 3 keV was determined, the 1^{-} state

$$|1^{-}\rangle = \alpha|\phi^{-}\rangle + \beta|\phi^{+}\rangle \tag{6}$$

exhibits an opposite parity admixture of $\beta \approx \langle PNC \rangle / \Delta E = 3 \times 10^{-4}$, where $\phi^{\pm}$ denote the unperturbed $1^{\pm}$ states.

One possibility to measure such a small admixture is to excite exclusively the 1^{-} state using a 100% linearly polarized γ-ray beam. By placing a sufficiently-thick absorber made of ^{20}Ne in beam, no gammas are available after the absorption process to excite the $T = 1, 1^{+}$ the excitation of which is ≈ 50 times larger than of the $T = 1, 1^{-}$ state.

Placing detectors perpendicular to the beam axis one could measure the M1 admixture of the de-excitation process

$$\langle 0^{+}|T(M1) + T(E1)|1^{-}\rangle = \alpha\langle 0^{+}|T(E1)|\phi^{-}\rangle + \beta\langle 0^{+}|T(M1)|\phi^{+}\rangle \tag{7}$$

since the E1(M1) NRF photons are emitted preferably perpendicular (parallel) to the polarization plane.

2.3. CONSTRAINTS ON $0\nu\beta\beta$-DECAY MATRIX ELEMENTS: A NOVEL DECAY CHANNEL OF THE SCISSORS MODE OF ^{150}SM

The existence of massive neutrinos has been established [42] from neutrino-oscillation experiments. Information on their particle character, either Dirac or Majorana, and their mass could be drawn [43] from a possible observation of neutrino-less double-beta ($0\nu\beta\beta$) decays, where a pair of protons (neutrons) converts simultaneously into a pair of neutrons (protons), and from the measurement of the corresponding transition rates

$$\lambda_{0\nu\beta\beta} = G_{0\nu}|M^{(0\nu)}|^2 \left(\frac{\langle m_\nu \rangle}{m_e}\right)^2 \tag{8}$$

Here, $\langle m_\nu \rangle = \sum_k |U_{\nu k}|^2$ is the average neutrino mass and $G_{0\nu}$ is a kinematical factor.

Several experiments to detect $0\nu\beta\beta$ decays are currently performed (CUORICINO, DCBA, EXO, GERDA, KamLAND-Zen, SNemo). Nevertheless, for a determination of the neutrino mass, the nuclear matrix element (NME) $M^{(0\nu)}$ needs to be calculated sufficiently precisely from nuclear structure theory. One of the most promising candidates to study possible $0\nu\beta\beta$ events is the nucleus ^{150}Nd. In the interacting boson model (IBM) the largest transition rate for $^{150}\text{Nd} \rightarrow {}^{150}\text{Sm}$ $0\nu\beta\beta$ was reported [44].

The phenomenological parameters of the IBM-2 Hamiltonian must be fitted to sufficiently sensitive data. For a reliable description of $\beta\beta$-reactions it is particularly important to verify the proper relative contributions of proton and neutron bosons to the IBM-2 wave functions. The nuclear $J^\pi = 1^+$ scissors mode is particularly sensitive to the proton-neutron coupling terms in the IBM-2 Hamiltonian and can be used to exclusively restrict the three parameters of the Majorana-interaction in the IBM-2 Hamiltonian. The spectroscopic properties of the $J^\pi = 1^+$ scissors mode states of ^{150}Sm, including their excitation energies and electromagnetic decay behavior, are mandatory for a sensitive test of IBM-2 Hamiltonians used for the description of $M^{(0\nu)}$. Recently, it was shown that the weak decay branches of the $J^\pi = 1^+$ scissors mode state to the first excited 0^+ state of ^{154}Gd has a large impact on the IBM-2 NME for the $0\nu\beta\beta$ decay of ^{154}Sm to the 0_2^+ state of ^{154}Gd [45].

The low-lying dipole strength of ^{150}Sm has been measured using bremsstrahlung photons [46]. However, no parity information on the $J = 1$ states at 2.5-4.0 MeV excitation energy is known and additionally small decay branching ratios of the scissors mode state in the order of 1% to the 0_2^+ state are available.

An intense, linearly polarized photon flux with a small bandwidth as provided by ELI-NP is necessary to determine parities and small decay branching ratios. The

possible $J^\pi = 1^+$ scissors mode states of ^{150}Sm have a ground-state decay width Γ_0 of 10-50 meV.

2.4. PROTON-NEUTRON SYMMETRY BREAKING IN NUCLEI: ROTATIONAL 2^+ STATES OF THE NUCLEAR SCISSORS MODE

The nuclear scissors (SC) mode is an isovector excitation mode found in deformed nuclei at about 3 MeV excitation energy (see e.g. [47] and references therein). In even-even nuclei, the $K = 1, 1^+_{SC}$ states are connected by strong M1 transitions to the ground-state band.It is expected that the 1^+_{SC} states are heads of a rotational bands build on top of it. However, members of those rotational bands have never been observed, yet. Since the moment of inertia of the rotational scissors mode band will be comparable to the ground state band, 2^+_{SC} states are located roughly $\Delta E = \frac{2}{3}E(2^+_1)$ above the 1^+_{SC} states in the 2.9-3.2 MeV range. In nuclear resonance fluorescence experiments the 2^+_{SC} state can be excited directly by E2 transitions which are expected to be in the order of 1 W.u. The ELI-NP γ-ray setup will reach a population of such a 2^+state of about 0.1/s for a deformed A≈150 nucleus and 0.2 g/cm^2 target mass.

The 2^+_{SC} state will predominantly decay to the 2^+_1 state by a M1 transition. Experimental identification of the 2^+_{SC} state needs to determine spin and parity and to measure the multipole mixing ratio of the $2^+_{SC} \rightarrow 2^+_1$ transition (Fig. 7). Therefore, γ decays have to be measured at (θ, ϕ) =$(90°, 0°)$, $(90°, 90°)$, $(135°, 0°)$, and $(135°, 90°)$ relative to the incoming beam and polarization axis, respectively. Additionally, an intense γ-ray beam is necessary for sufficiently high population of a weakly excited 2^+ state.

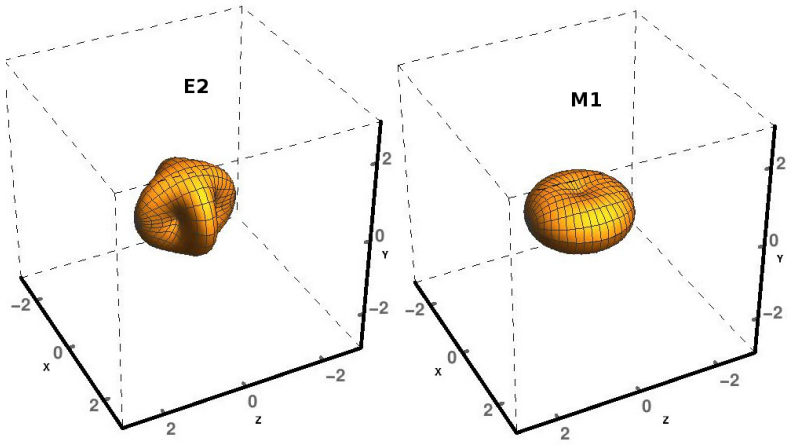

Figure 7 – Angular distribution of a $0^+ \rightarrow 2^+ \rightarrow 2^+$ sequence for a pure E2 (left) and M1 (right) decay. The beam axis is along the z axis; the polarization vector is along the x axis.

2.5. ELECTRIC AND MAGNETIC DIPOLE MOMENTS IN ATOMIC NUCLEI: THE LOW-ENERGY DIPOLE RESPONSE OF HEAVY RADIOACTIVE NUCLEI

The photoresponse of actinide nuclei is especially interesting from a nuclear structure point of view: recently a strong static octupole deformation has been observed in the nucleus ^{224}Ra. This means a breaking of the reflection symmetry and may even help to search for physics beyond the standard model [48]. A coupling of an octupole mode to a quadrupole deformed core (as it is the case for actinide nuclei) leads to enhanced electric dipole strength which can be detected by measuring the detailed E1 photoresponse of the nucleus at low energies.

Another phenomenon recently discovered in a number of actinide nuclei is the observation of unexpectedly high magnetic dipole strength in the order of 12 μ_N^2 at energies between 1 and 3.5 MeV in actinides which is interpreted as a scissors-like resonance [49]. Again photon scattering on actinides could help to understand this M1 enhancement compared to typical ground state M1 strength found in other deformed nuclei.

Finally, the detailed knowledge of the fingerprint of actinides in photon scattering has important applications in homeland security and the analysis of spent nuclear fuel due to the high penetrability of the photon probe [50–52], see the TDR on applications [53] as well.

However, NRF experiments on actinides are very challenging, partly due to the very low amounts of available target materials and partly due to the natural activity of the samples producing large background in the γ-ray detectors. The high luminosity of ELI-NP will allow for detailed NRF investigations of many radioactive nuclei for the first time. Typical beam energies needed are in the range from 0.5 to 5.0 MeV. Determination of the photo-response of the actinide nuclei ^{236,237}Np, ^{240}Pu, ^{243}Am, and ^{248}Cm by performing an energy scan would be possible as day-one experiments at ELI-NP.

2.6. THE ORIGIN OF MATTER: STUDIES OF THE PHOTO-RESPONSE OF WEAKLY-ABUNDANT NUCLEI NEAR THE N=82 SHELL CLOSURE

The low-lying dipole strength in nuclei with a very low natural abundance, as for example the p-nuclei which are produced in astrophysical scenarios different from the standard s and r process, is in many cases unknown. Large amounts of highly-enriched target material would be needed to investigate the dipole strength with a reasonable sensitivity and measuring time at existing facilities. Using the high-intensity, mono-energetic, and linearly polarized gamma-ray beam which will be provided at ELI-NP, a slightly enriched target material in low quantity will be sufficient for studying the dipole response in real-photon scattering experiments. In addition to strength distributions, parities can be deduced at the same time, allowing

for a clear distinction of magnetic and electric dipole excitations.

The low-lying E1 strength for ^{140}Ce that is the cerium isotope with the highest natural abundance (88.45%) is well-known. However, there are two low-abundant p-nuclei in the cerium chain, namely ^{136}Ce and ^{138}Ce with natural abundances of 0.19% and 0.25%, respectively. The dipole response of these nuclei could be measured for the first time at ELI-NP. This would allow to discuss the development of E1 strength in dependence of the neutron number. As a special case, one could search for the two-phonon 1^- state and its decay. This state stems from the coupling of the first 2^+ to the first 3^- state, which is usually located at an energy of around 90% of the sum of the level energies of the constituent states. This means in ^{136}Ce a two-phonon candidate would be located around 2763 keV and in ^{138}Ce around 2863 keV.

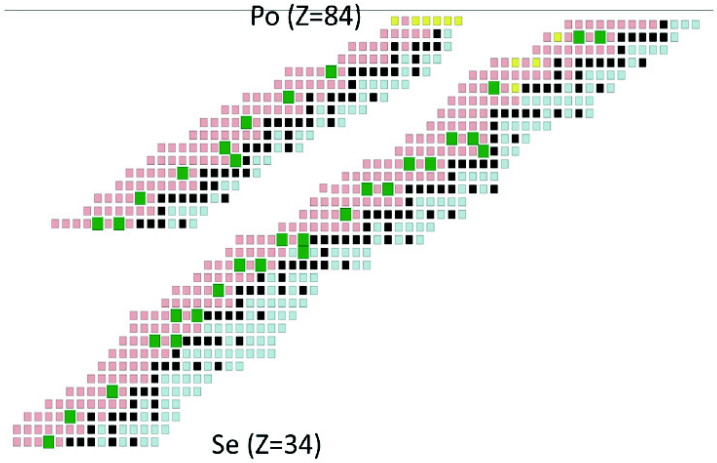

Figure 8 – About 35 stable heavy isotopes on the proton rich side of the valley of stability are bypassed by the s and r processes of nucleosynthesis. They are believed to be produced in the so called p process. Most of these nuclides have very low natural abundance.

2.7. MODEL AND CALIBRATION INDEPENDENT WIDTH DETERMINATION AT ELI-NP: SELF-ABSORPTION MEASUREMENTS

The method of self-absorption [1, 54] allows to study absolute values for the ground-state transition width Γ_0 in a model-independent way. The beam intensity passing an absorber target made of the material of interest at the resonance energy is compared to the beam intensity without absorber target. A so-called scatterer target made of the same material as the absorber serves as analyzer for the beam intensity. When the beam intensity becomes lower, the number of scattered photons

also decreases. Thus, the difference of resonantly scattered photons in the scatterer is a measure for the ground-state transition width.

Since self-absorption measurements are relative measurements they allow for the investigation of ground-state transition widths, i.e. lifetimes of nuclear levels, with very high accuracy. Thus, they offer the opportunity to perform high-precision measurements of absolute lifetimes of calibration standards used for NRF measurements such as ^{11}B and ^{27}Al. Nowadays, NRF with bremsstrahlung is a standard approach to investigate low-lying dipole strength, such as the scissors mode or the Pygmy Dipole Resonance [29]. However, despite of the Schiff formula [55] in the limit of infinitesimal thin radiators, a closed formula describing the spectral distribution of the bremsstrahlung is not available. Therefore, in most experiments with bremsstrahlung, an independent photon-flux calibration is necessary.

The lifetimes of the four lowest-lying levels of ^{11}B that are used for photon-flux calibrations in NRF are known with accuracy between 3.4 and 9.1% [56]. A self-absorption measurement on ^{11}B at the NRF setup at ELI-NP would result in much more precise lifetimes: with the setup specifications given in the TDR, a $m = 1$ g ^{11}B scatterer, a $m = 1$ g ^{11}B absorber and a total measuring time of 24 h, an accuracy of about 1.0% for the lifetimes can be easily achieved. The entire NRF community will profit from this achievement and will be able to produce more precise results, e.g. for transition strengths.

In combination with standard NRF measurements that are sensitive to the product of the ground-state transition width Γ_0 and the branching ratio Γ_0/Γ self-absorption measurements allow also to study branching ratios to the ground state for individual excited states and, thus, to investigate, e.g., the decay pattern of the PDR.

Previous investigations of the PDR assumed either an exclusive decay of the PDR states to the nuclear ground state ($\Gamma_0/\Gamma_1 \approx 1$) or they had to rely on a pure statistical description of the decay strengths to lower-lying excited states. Recently, Tonchev and co-workers studied a mean branching ratio to the ground-state for states of ^{138}Ba excited in 300 keV wide energy bins and showed that the decay via intermediate states cannot be neglected [28]. Similar investigations of ^{60}Ni [57], ^{94}Mo [58], and ^{130}Te [59] confirmed this observation. In the cases of ^{94}Mo and ^{130}Te the mean branching ratios to the ground state were compared to simulations within the statistical model, revealing that a pure statistical description of the decay behavior underestimates the experimental data. Thus, investigations of the PDR exploiting the statistical model may systematically overestimate the decay strengths. On the other hand, the strength is underestimated when $\Gamma_0/\Gamma_1 \approx 1$ is assumed.

Therefore, for a more precise investigation and a deeper understanding of the PDR and its decay pattern information on both, the excitation width Γ_0 of the PDR from the ground state, as well as the total transition width Γ is needed for individual states.

To investigate the decay pattern of individual states the method of relative self-absorption can be used. A very recent measurement at the DHIPS measuring site at TU Darmstadt, Germany on ^{140}Ce showed that the method works very well. However, due to the rather large background radiation at DHIPS and the limited photon flux the measurement was sensitive only to rather strongly excited states. Most of these states decay - as expected - almost exclusively directly to the ground state. However, the weaker excited states are expected to exhibit rather large branching to intermediate states. However, since they have only a small excitation width Γ_0 a setup with high photon flux and low background radiation such as the NRF setup at ELI-NP is needed to investigate the states with $\Gamma_0 < \Gamma_1$.

3. TECHNICAL PROPOSAL

The main experimental setup for NRF measurements consists of an array of gamma-ray detectors. Different types of detectors will be used in order to maximize the solid angle covered with the detectors placed in close geometry around the target, and the total photopeak efficiency of the array, to optimize the response of the array to gamma-rays of different energies from few hundred keV to several MeV, and to allow for precise gamma-ray polarization and angular distribution measurements. The array will consist of large volume HPGe detectors of the CLOVER type and large volume $LaBr_3$ scintillator detectors.

3.1. LOCATION OF THE EXPERIMENTAL SETUP

According to the division of the gamma beam system into two sections, low- and high-energy, there are two main locations considered for the NRF (-based) experiments. Experiments with gamma rays up to 3.5 MeV will be performed in the experimental area **E2** while experiments with higher energy gamma rays, up to 19.5 MeV, will be performed in the experimental area **E8**. One can still maintain the possibility to perform experiments with low-energy gamma beams in the **E8** area. In the **E2** area the array will also be used for applied physics experiments (as discussed in the dedicated TDR). The foreseen locations of the array are shown in Fig. 9. The layout of the Gamma Beam System (GBS) and the experimental areas with gamma beams are shown in this figure as well. The design of the array has to take into account the possibility to move the array and the associated infrastructure in the different locations for the experimental activities.

The **E2** area is located in the Accelerator Bay 2 that also hosts the high-energy stage of the electron accelerator. The distance between the axes of the low-energy gamma beam line and the electron beam line is 1.8 m at the beginning of the bay and it increases to 2.1 m at the end of the bay. The transversal dimensions of the array are

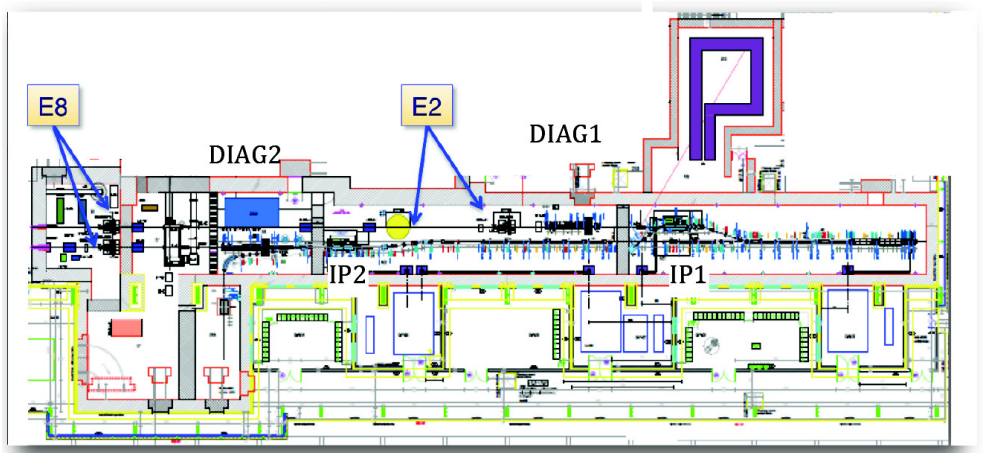

Figure 9 – The locations of the NRF gamma-ray array in the two experimental vaults **E2** (low-energy gamma-ray beams) and **E8** (high-energy gamma-ray beams).

limited by the distance between the gamma and electron beam lines and the height of the gamma beam line of 1.5 m from the floor. The array will be placed downstream from primary collimator and the gamma beam characterization equipment (DIAG1). This means that the minimum distance from the low-energy interaction point (IP1) to the NRF target is of about 20 m.

The **E8** area will be shared among all the experiments using gamma beams. This area will be reached by both the low-energy and the high-energy gamma beams. The available space will be divided among the experimental setups and different beam diagnostics and monitor devices. The infrastructure related to the ELIADE array has to be designed such to allow for the translation of the whole setup from one beam line to the other. The minimum distance between the high-energy interaction point (IP2) and the target position is about 25 m. For the low-energy beam line the target will be located about 60 m away from IP1.

Additional equipment for the beam characterization and monitoring will be used during the experiments and it will be provided as described in the TDR for the Gamma Beam Delivery and Diagnostics [66]. The information from these devices will be integrated in the data flux and recorded synchronized with the experimental data.

3.2. THE γ-RAY DETECTOR ARRAY ELIADE

The gamma-ray array for the NRF measurements, called **ELIADE** (**ELI**-NP **A**rray of **DE**tectors), will comprise 8 CLOVER Ge detectors. The CLOVER detectors are built of 4 single HPGe crystals mounted in the same cryostat. Each crystal will be tapered parallel to its axis in order to allow for a close and compact assembly

to the other crystals and a conical tapering at the front part will allow for a close geometry packing of the detectors. An example of such CLOVER geometry is shown in Fig. 10.

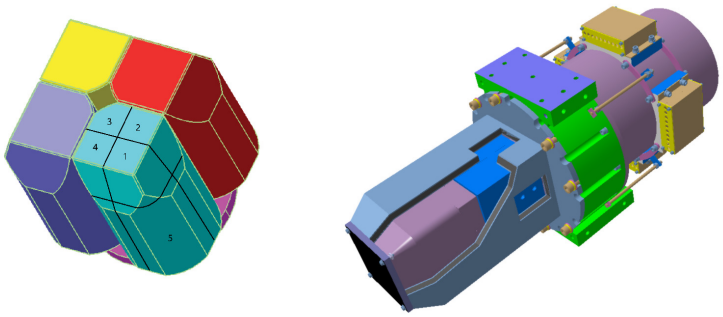

Figure 10 – The CLOVER detector crystals geometry. On the left side, the segmentation is shown for one of the crystals. The CAD design of the ELIADE CLOVER detectors is shown on the right-hand side.

The CLOVER detectors will be placed on two rings: one allowing the positioning of the detectors at azimuthal angles between 90° and 98° , and another one fixed at 135°. The detectors will be retractable, a feature that will serve to enable a certain optimization of the geometry upon the actual experimental conditions. The minimal distance to the target is of the order of 15 cm. The effective angles of the CLOVER crystals at the shortest distance will be: 81°-89°, 99°-107°, 126° and 144°. As it can be seen the CLOVER detectors ensure in a natural way the possibility to measure angular distributions of the emitted gamma rays. In choosing this geometry care was taken to avoid placement of detectors at forward angles where Compton and atomic scattering processes of the beam off the target would blind the detectors. This type of HPGe detector and the configuration has been selected on the basis of the existing experience with CLOVER detectors at previous large arrays for gamma-ray spectroscopy such as EUROBALL, VEGA, EXOGAM, TIGRESS, YRAST-Ball, TASISpec, etc. [60–64]. The layout of the CLOVER detectors in the ELIADE array is shown in Fig. 11. In between the detectors at 90° one can place large volume $LaBr_3$ scintillator detectors (e.g., 3x3) for the efficient detection of high-energy gamma rays. These detectors would stay at polar angles making 45° with the CLOVER detectors. The space left in these positions can fit detectors with dimensions similar to the CLOVER detectors. The mechanical support frame is designed in such a way to allow for the rotation of the structure at 90° to bring the $LaBr_3$ detectors at the angles relevant for polarization measurements by rotating the

structure by 45 ° .

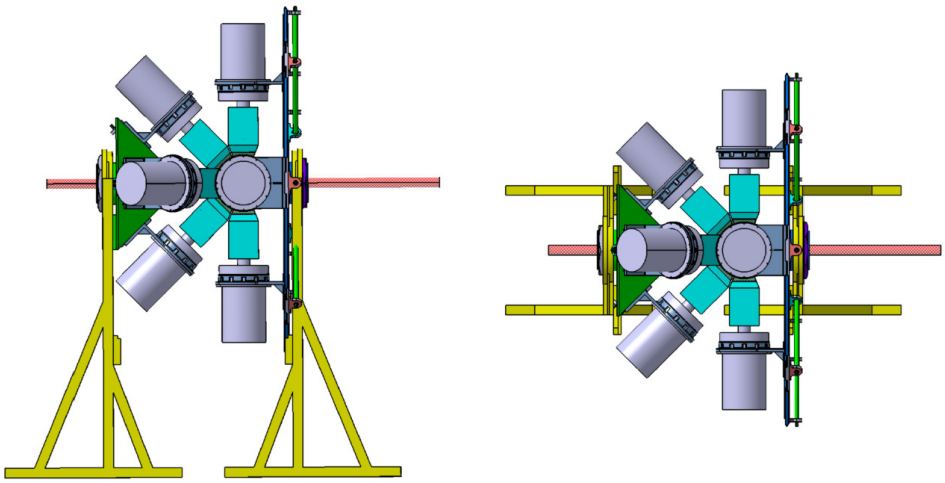

Figure 11 – A simplified sketch of the ELIADE array: side-view on the left-hand side and top view on the right-hand side. The array is composed of 8 CLOVER detectors, four at 90° and four at 135°. At 90° one can mount four additional detectors (large volume $LaBr_3$ scintillator detectors or CLOVER detectors are considered) at 45° with respect to the CLOVER detectors in the standard configuration.

3.2.1. The CLOVER detectors

The CLOVER detector type proposed for the ELIADE array is to have the size of EXOGAM or TIGRESS CLOVER detectors where each of the four n-type HPGe crystals has a diameter of 60 mm and a length of 90 mm before machining with flat surfaces on four sides (see Fig. 10 for details). Two adjacent sides are tapered at 22.5° over 30 mm from the front of the crystal to allow the mounting of the detectors in close assembly [62]. The crystals in the CLOVER cryostat are assembled close together with an electric insulation between them that allows them to be operated at different bias voltages. The separate bias voltage for each crystal improves noise immunity and allows to operate at lower than the operational voltage should it be needed.

The crystals are installed in a common vacuum cryostat as shown in Fig.10. A low absorbing constructive material (Al alloy) is also to be used for this purpose. The germanium crystals are of n-type HPGe and have typical properties (impurity concentration between 0.5 and 1.2 x 10 10 at/cm^3 and the major impurities carriers lifetime of < 5 ms) for this type of detectors and are to be operated at bias voltage less than 5000 V. Table 1 summarizes the expected properties of the CLOVER detector.

The crystal assembly in CLOVER configuration is supposed to be annealing

Table 1

Properties of the CLOVER HPGe crystals

Depletion voltage, Vd	$<$ 3000 V
Operational voltage	$\geq$ Vd+1000 V
Maximal operational voltage	5000 V
Relative efficiency @ 1.3 MeV at 25 cm	$\geq$ 38%
Energy resolution at 1.3 MeV (6 μs shaping time)	$\leq$ 2.35 keV
Energy resolution at 122 keV (6 μs shaping time)	$\leq$ 1.35 keV
Line shape FWTM/FWHM	$\leq$ 1.95
Sensitivity	100 mV/MeV
Holding time	$\geq$ 20 h

qualified, which implies careful selection of the plastic materials used in the assembly. The detector has integrated heating elements mainly to be used for vacuum conditioning and 2 PT100 sensors - one at the crystal holder and one at the absorber container. The last one drives a bias shutdown card providing a safe shutdown of the bias in case of unexpected warming up. The efficiency of the CLOVER detectors is much improved by the add-back procedure of summing together the individual gamma-ray releases of energy in all four crystals. The relative efficiency of the CLOVER detector composed of four crystals is augmented through this procedure to about 200% @ 1.3 MeV, significantly higher than the simple sum of the individual efficiencies of the four crystals (about 160%). This feature is of particular importance for the detection of high-energy gamma rays.

3.2.2. GEANT4 simulation of the ELIADE array

The geometry of the CLOVER detectors was implemented in a GEANT4 [65] simulation using as a starting point the dimensions of the segmented CLOVER detectors at TIGRESS [63]. Fig. 12 illustrates the geometry of the CLOVER detectors as defined in the GEANT4 simulation package.

The full ELIADE array was also implemented in the simulation package. The geometry chosen for the calculations is the one with four segmented CLOVER detectors at 98° and four segmented CLOVER detectors at 135° (Fig. 13).

Within the simulation package the influence of the add-back procedure on the detection efficiency of high-energy photons was investigated. This was done by studying the number of counts in the photopeak of a spectrum obtained in one segment versus the number of counts in the photopeak of the spectrum obtained by applying the add-back procedure at crystal level (Fig. 14 bottom spectrum). The same can be done at CLOVER level by comparing the add-back spectrum with the spectrum in individual crystals (Fig. 14 upper spectrum). Fig. 14 illustrates the re-

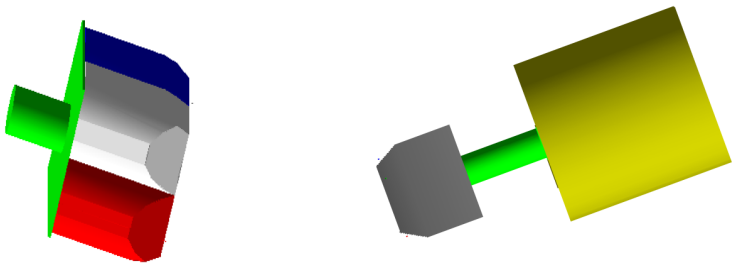

Figure 12 – A CLOVER Ge detector simulated with GEANT4. The geometry of the crystals and the dimensions of the cryostat are those of the TIGRESS detectors [63]. This is a simplified geometry as compared to the CAD model shown in Fig. 10.

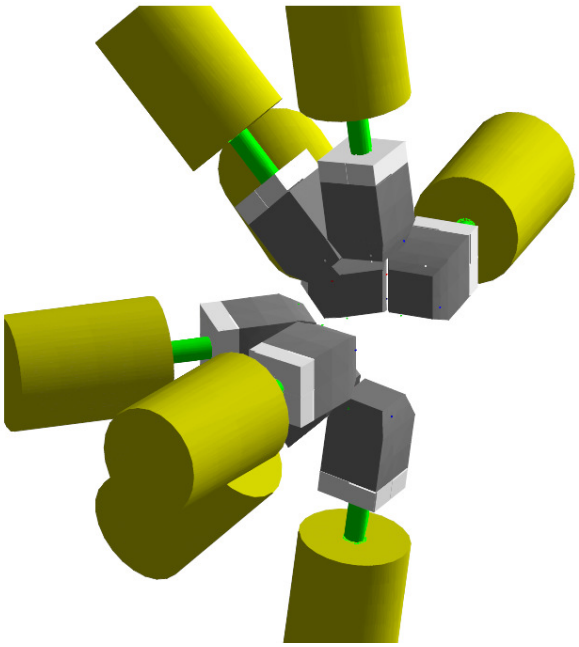

Figure 13 – The ELIADE array simulated in GEANT4. Four segmented CLOVER detectors were placed at 98° and other four at 135°.

markable improvement in the photopeak area when add-back is applied.

The detection of the NRF gamma rays is hindered by the background radiation originating from the Compton scattering of the gamma beam on the target material and from the annihilation of the positrons produced in the target. Fig. 15 shows the

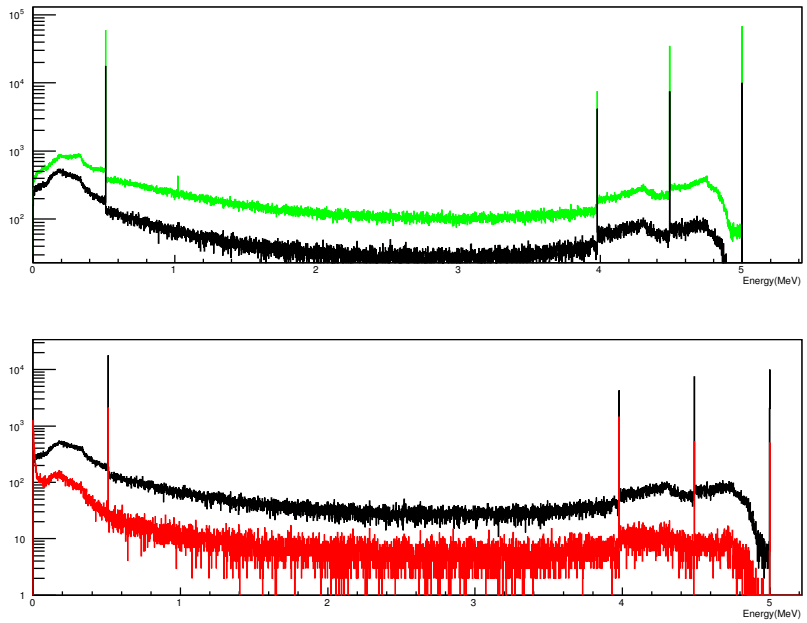

Figure 14 – Illustration of the add-back effect on the photopeak efficiency in the case of a segmented CLOVER detector. The simulations were done in GEANT4 for a 5 MeV gamma ray emitted from the target position. The bottom spectrum compares the spectrum recorded in one segment (red) with the spectrum obtained from adding-back the energy releases in all the segments (black) from the same crystal. The upper spectrum compares the add-back on the whole CLOVER detector (green) with the spectrum from a single crystal (black). The improvement of the full energy peak as compared to the single- and double-escape peaks is evident.

distribution of the Compton scattered gamma beam as a function of the angle for an incident gamma beam of 7 MeV. It can be noticed that the detectors at 90° will mainly see Compton scattered gamma rays with energies around 500 keV while the detectors at 135° will mainly see Compton scattered gamma rays with energy around 250 keV. The annihilation gamma rays of 511 keV are distributed uniformly over the whole solid angle.

Due to the particular time structure of the gamma beams at ELI-NP (Fig. 16) with macrobunches 496 ns long repeating every 10 ms and 1 ps microbunches containing about 10^5 photons repeating every 16 ns, the number of events per macrobunch that the detectors can handle are limited. Typical peaking time for the energy filters in the case of Ge signals is of the order of about 10 μs and, consequently, there can be only one event detected for every macrobunch. While the number of events from the NRF processes is low enough, the events from the background radiation can produce significant pile-up.

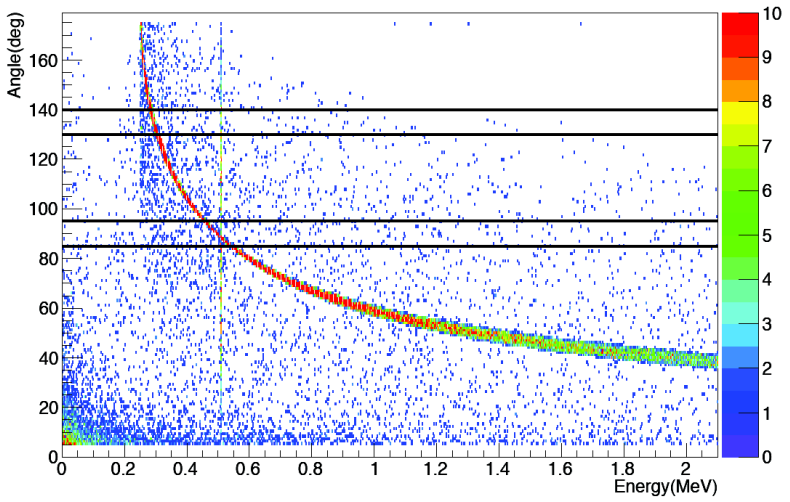

Figure 15 – Energy distribution of the Compton scattered gamma beam as a function of the scattering angle. The two bands shown on the figure are indicating the angular coverage of the detectors placed at 90° and 135° . At 90° the background events are concentrated around 500 keV while at 135° it is around 250 keV.

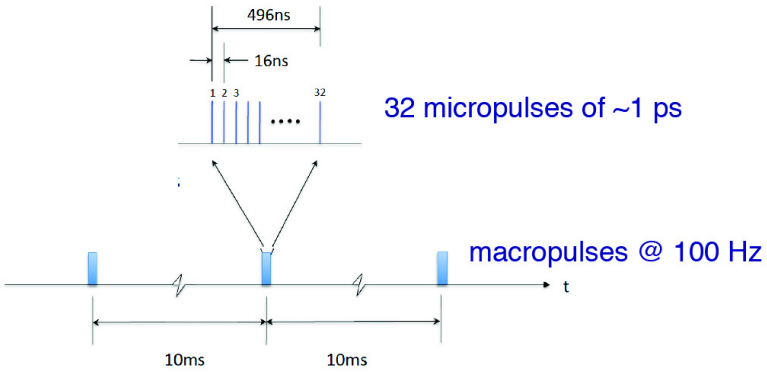

Figure 16 – Time distribution of the gamma beam at ELI-NP. The macrobunch repeating at every 10 ms are composed of 32 microbunch each with a duration of about 1 ps and separated by 16 ns from one another. Every microbunch contains about 10^5 gamma-ray photons.

One way to reduce the radiation background on the detectors is to increase the distance between the detectors and the target with a subsequent reduction of the solid angle subtended by the detectors. This method, unfortunately, leads to the reduction of the detection efficiency also for the NRF gamma rays of interest. When the gamma rays of interest are of high energy, one can reduce the low-energy background radi-

ation, below 500 keV, by placing Pb and Cu absorbers in front of the detectors. The influence of using a thick Pb shield in front of the detectors was studied in GEANT4 by calculating the CLOVER detector response to photons with energies between 500 keV and 5 MeV emitted from the center of the array. The results of the simulations are shown in Fig. 17. The importance of these absorbers is well-known from other NRF setups.

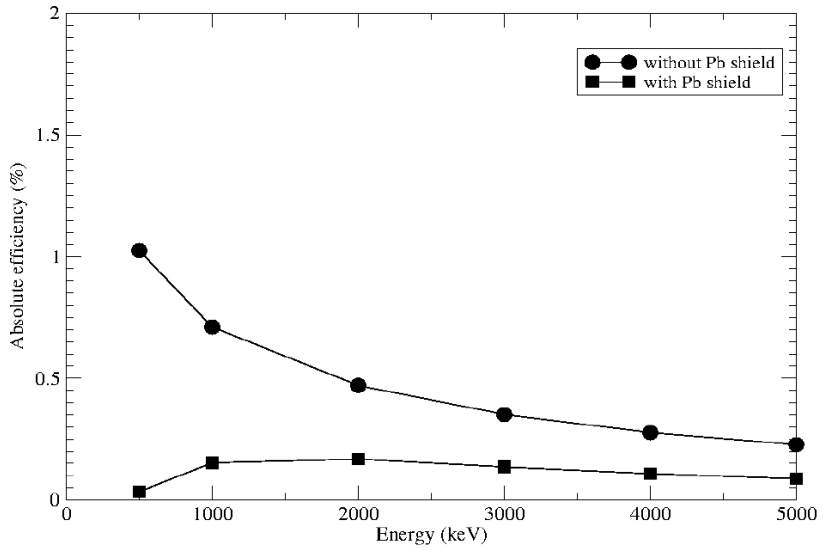

Figure 17 – GEANT4 simulation of the CLOVER detectors response to photons with energies between 500 keV and 5 MeV with (filled squares) and without (filled circles) a 2 cm thick Pb absorber in front of the detector.

The absolute efficiencies and the peak-to-total (P/T) ratios are plotted as a function of the photons energy with and without a 2 cm Pb absorber placed in front of the Ge detectors. It can be seen from Fig. 17 and Fig. 18 that the Pb absorber can efficiently reduce the gamma-ray radiation background with energy below 500 keV but at the cost of a drastic reduction of the absolute detection efficiency up to high energies and a significant degradation of the gamma-ray spectra quality reflected in a lowering of the P/T values.

The methods for reducing the radiation background are leading to a reduction of the advantage of having a high brilliance gamma beam. In order to take full benefit of the gamma beam features and of the high detection efficiency for gamma rays the present TDR proposes the use of segmented CLOVER detectors.

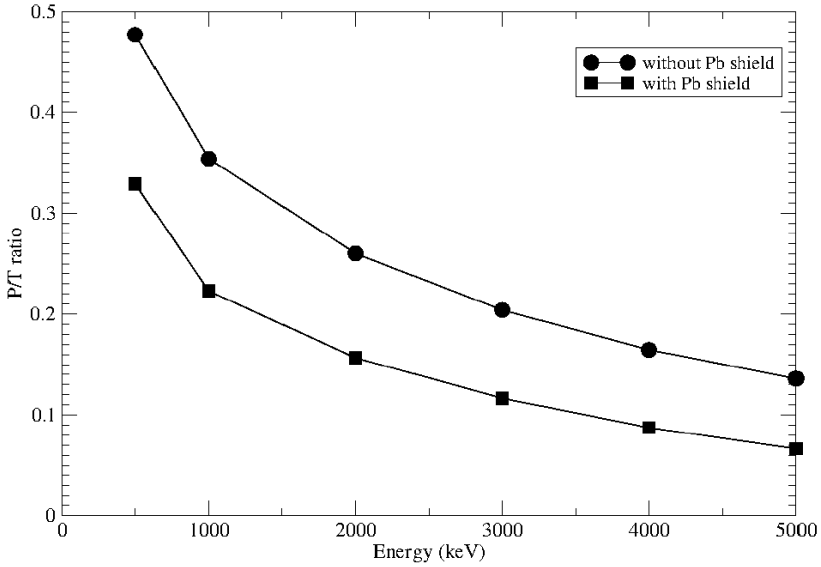

Figure 18 – GEANT4 simulation of the CLOVER detectors response to photons with energies between 500 keV and 5 MeV with (filled squares) and without (filled circles) a 2 cm thick Pb absorber in front of the detector.

3.2.3. Use of segmented CLOVER Ge detectors

Premises:

- need of high efficiency detection over a wide range of gamma-ray energies (0.5 - 20 MeV), combined with high energy resolution hence
  large-volume HPGe detector is the only valid option

Table 2

Detector type	Relative efficiency	Cost	# of channels
Large volume HPGe	200%	200 kEuro	2
CLOVER detector	200%	280 kEuro	8
Segmented CLOVER detector	200%	380 kEuro	34

- typical experiments

  1. Measure at a certain known resonance (long experiment possible)
  2. Scan the energy range for new resonances:
     0.5 - 3 MeV range, 10 keV bandwidth - 250 scan positions

0.5 - 20 MeV range: 10 keV bandwidth - 1900 scan positions

detection rates should be maximized to keep experiments duration within reasonable limits

- expected radiation:
  - NRF gamma rays: few hundred barn in meV range widths + thermal induced Doppler shift lead to 1 - 100 eV·b integrated cross-section over a few eV. This translates to 4 - 10 times more than the absolute cross-section for the classical effects (Compton scattering, pair production, photoelectric effect, ...) for the same energy range. Nevertheless, the bandwidth of the gamma beam is of the order of a few keV and consequently the rates coming from the NRF (which is produced only over few eV) becomes orders of magnitude lower than that of the other effects;
  - Compton scattered gamma beam: the energy of Compton scattered gamma rays decreases with increasing angle; the scattering probability decreases with decreasing angle (and increasing energy);
  - Gamma rays of 511 keV: from the annihilation of the positrons produced by the gamma beam through pair production; these gamma rays are isotropically emitted from the target position
- beam time structure: 32 microbunches of gamma rays at 16 ns apart with a repetition rate of 100 macrobunches /s
- response time of the Ge detectors: the rise time of the HPGe detectors is of the order of 100 - 500 ns, depending on the size/shape of the Ge crystals. If two photons coming from the same macrobunch reach the same detector they will be detected as pile-up (they will not be measured as two different photons but as one photon with the sum energy of the two original photons).

Conclusion: the maximum sustainable rate for measurements is 100 Hz that is one event from each macropulse.

In order to avoid the pile-up conditions, the rate in each detector (or crystal, or segment) needs to be around 1 for each macrobunch. That means that the mean rate should be around 0.3 to reduce the amount of pile-up to negligible levels. This translates to maximum rates of one detected photon/macrobunch for a large HPGe detector, four detected photons/macrobunch for a CLOVER detector, higher than 16 photons/macrobunch for a segmented CLOVER (provided the 16 photons are of low energy, they are deposited in the frontal segments of the detector and leave the back segments available for high energy photons).

Case study 1

Gamma rays following NRF, Compton scattering and positron annihilation are emitted from target. The lead absorbers in front of detectors preferentially filter out the Compton scattered gamma beam and 511 keV γ rays due to their lower energy than the NRF photons. This leads to the need to have as many NRF photons emitted from the target, so that by relative filtering the ratio NRF/(Compton+511) to be as high as possible.

NRF in ^{238}U: known resonances around 2.1 MeV

- Beam: 10^8 photons within bandwidth/s; 30000 ph/s/eV
- Target: diameter: 0.5 cm (estimated beam diameter at target position)
- Detector: segmented CLOVER, efficiency and P/T from the simulations (0.45% photopeak efficiency at 2.1 MeV, 0.25 P/T ratio).

Note: we will talk about the number of detected photons and not about the photopeak efficiency, as the pile-up with a partially detected photon is even more destructive than the pile-up with a fully deposited one (which leads to a sum peak, with a known probability).

Fig. 19 illustrates the variation of the number of detected NRF photons/s with target thickness. It can be seen that as the number of photons in the resonance area is depleted by passage through the target. The addition of extra thickness does not increase the number of available photons. The thickness of the target should be chosen in the rapid ramp region of the curve. A value of 0.5 cm is chosen for these calculations, although optimizations around this value can be made. This thickness corresponds to a target of roughly 0.5 g assuming a beam diameter of 5 mm.

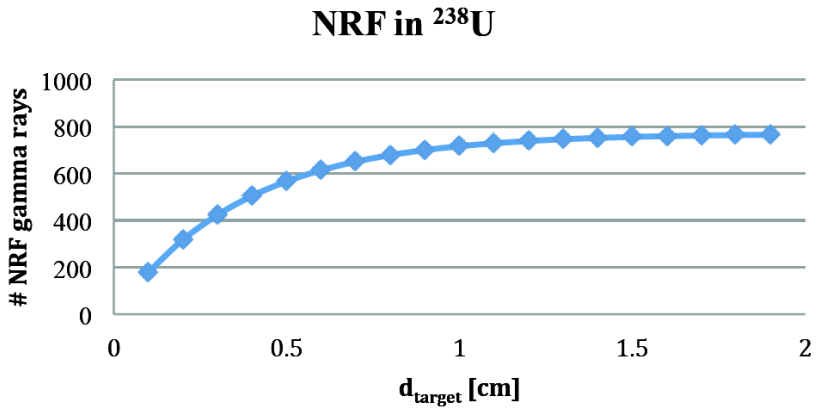

Figure 19 – Calculated yield of NRF gamma rays in ^{238}U as a function of the target thickness.

Under these experimental conditions, the number of photons detected by a single detector without Pb absorber (thick target assumption, all positrons are annihilated) is shown in the table below:

Table 3

Source	Energy (MeV)	Number of photons/sec
NRF	2.1	566
Compton towards the ring at 98°	0.36	61966
Compton towards the ring at 135°	0.26	43359
annihilation	0.511	59020

Table 4 summarizes the variation of the number of gamma rays per second detected by the CLOVER detector as a function of the thickness of the lead shield in front of the detector.

Conclusions case study 1:

- By using a large volume HPGe one can measure with a 3.5 - 4 cm thick Pb shield in front of the detector and only be able to measure less than 100 NRF photons/second;

- By using a CLOVER detector one can measure with a 2.7 - 3.3 cm thick Pb shield in front of the detector and detect about 130 NRF photons/second;

- With a segmented CLOVER detector the thickness of the Pb shield can be reduced to about 2 cm shield resulting in the detection of about 200 NRF photons/second;

Table 4

Variation of the number of gamma rays per second detected by the CLOVER detector as a function of the thickness of the lead shield in front of the detector for case study 1

Pb shield thickness [cm]	NRF [counts]	Compton 98° [counts]	Compton 135° [counts]	Annihilation [counts]
1.2	303	64	0	6573
1.6	246	6	0	3162
1.7	233	4	0	2634
1.8	221	2	0	2193
1.9	210	1	0	1827
2.0	199	1	0	1521
2.1	189	0	0	1267
2.2	180	0	0	1055
2.3	171	0	0	879
2.4	162	0	0	732
2.5	154	0	0	610
2.6	146	0	0	508
2.7	138	0	0	423
2.8	131	0	0	352
2.9	125	0	0	293
3.0	118	0	0	244
3.1	112	0	0	203
3.2	107	0	0	169
3.3	101	0	0	141
3.4	96	0	0	118
3.5	91	0	0	98
3.6	86	0	0	82
3.7	82	0	0	68
3.8	78	0	0	57
3.9	74	0	0	47
4.0	70	0	0	39
4.1	67	0	0	33
4.2	63	0	0	27

Case study 2

Gamma rays following NRF, Compton scattering and positron annihilation are emitted from target. The thickness of the target is reduced such to maintain the count

rates at manageable levels with thinner lead absorbers in front of detectors.

NRF in ^{238}U: known resonances around 2.1 MeV

- Beam: 10^8 photons within bandwidth/s; 30000 ph/s/eV;
- Target: diameter: 0.5 cm (estimated beam diameter at target position)
- Detector: segmented CLOVER, efficiency and P/T from the simulations (0.45% photopeak efficiency at 2.1 MeV, 0.25 P/T ratio).

Note: we will talk about the number of detected photons and not about the photopeak efficiency, as the pile-up with a partially detected photon is even more destructive than the pile-up with a fully deposited one (which leads to a sum peak, with a known probability).

The thickness of the target is chosen at the smallest practical level. A value of 0.05 cm is chosen, although optimizations around this value can be made. This thickness corresponds to a target mass of roughly 0.1 g.

Table 5

Source	Energy (MeV)	Number of photons/sec
NRF	2.1	96
Compton towards the ring at 98°	0.36	6959
Compton towards the ring at 135°	0.26	4869
annihilation	0.511	6628

The table below summarizes the variation of the number of gamma rays per second detected by the CLOVER detector as a function of the thickness of the lead shield in front of the detector.

Conclusions case study 2:

- By using a large volume HPGe one can measure with a 2 - 3 cm thick Pb shield in front of the detector and only be able to measure less than 25 NRF photons/second;
- By using a CLOVER detector one can measure with a 1.6 - 2.2 cm thick Pb shield in front of the detector and detect about 40 NRF photons/second;
- With a segmented CLOVER detector the thickness of the Pb shield can be reduced to about 1 cm shield resulting in the detection of about 70 NRF photons/second;

Table 6

Variation of the number of gamma rays per second detected by the CLOVER detector as a function of the thickness of the lead shield in front of the detector for case study 2

Pb shield thickness [cm]	NRF [counts]	Compton 98° [counts]	Compton 135° [counts]	Annihilation [counts]
0.2	86	2210	225	4597
0.3	82	1245	48	3829
0.4	78	702	10	3189
0.5	74	396	2	2656
0.6	70	223	0	2212
0.7	67	126	0	1842
0.8	63	71	0	1534
0.9	60	40	0	1278
1.0	57	22	0	1064
1.1	54	13	0	886
1.2	51	7	0	738
1.3	49	4	0	615
1.4	46	2	0	512
1.5	44	1	0	426
1.6	42	1	0	355
1.7	39	0	0	296
1.8	37	0	0	246
1.9	36	0	0	205
2.0	34	0	0	171
2.1	32	0	0	142
2.2	30	0	0	118
2.3	29	0	0	99
2.4	27	0	0	82
2.5	26	0	0	68
2.6	25	0	0	57
2.7	23	0	0	47
2.8	22	0	0	40
2.9	21	0	0	33

Final conclusions:

- The segmented CLOVER detector is superior in performance in both extreme cases considered for the analysis. This is not unexpected if we compare the

photon induced reactions with a pulsed photon beam like ours to a very high multiplicity event in conventional experimental conditions. Of extra advantage in our case is the fact that the non-interesting photons (Compton scattered, annihilation) have low energies, so they can be stopped in the frontal segments of the detector.

- using a thick target and thick Pb absorber in front of the detectors is a favorable measurement type, regardless of the type of detector used.

The signals from the Ge detectors will be continuously digitized. As discussed in Ref. [63] the segmented CLOVER detectors possess some gamma-ray interactions position identification capabilities by using pulse shape analysis. By combining pulse shape analysis with the high probability to absorb the background radiation in the frontal segments one can develop algorithms to further reduce the pile-up of NRF events with background events while maintaining the Pb absorber in front of the detectors at small thickness.

3.2.4. Anti-Compton shields for the CLOVER detectors

The EXOGAM CLOVER detectors are fitted with Compton suppression shields. These shields are of modular type being composed of three different types of shields: a rear side shield made of BGO, a side shield made of BGO and a back catcher made of CsI(Tl). The CLOVER cryostats are fitted with holders for the modular anti-Compton shields.

In ELIADE configuration the detectors will be fitted with both active and passive shields. The back catchers will be used as active Compton suppression shields as the energy of the gamma rays to be detected in the proposed experiments is mostly high and these gamma rays predominantly scatter at small angles in forward direction. To protect the detectors of the gamma rays scattered from the neighboring detectors or from the surrounding materials passive shields made of lead, in the geometry of the side and rear side shields will be used.

3.2.5. $LaBr_3$(Ce) scintillator detectors

The mechanical support of ELIADE can hold 8 detectors at the 90° ring. The 4 additional detectors that can be placed at 45° with respect to the CLOVER detectors can be of the CLOVER type or $LaBr_3$(Ce) scintillator detectors. $LaBr_3$(Ce) scintillator detectors are a lower cost solution to complete the array with more detectors. A 3x3 $LaBr_3$(Ce) detector has a relative efficiency of about 165%. The higher efficiency for high-energy gamma rays will make these detectors extremely useful when studying gamma rays from the decay of Pygmy Dipole Resonances.

These detectors due to their faster time response can be operated, under the specific conditions of the ELI-NP gamma beam, to counting rates as high as 1000 Hz

(10 times more than the Ge detectors) with no significant pile-up. With a time resolution at the nanosecond level these detectors can separate gamma rays originating from different beam microbunches.

As for the Ge detectors one has to use passive shielding of these detectors to protect them from the scattered radiation off the surrounding materials. Lead absorbers will be used in front of the detectors to reduce the level of background radiation.

3.2.6. The mechanical support structure

The mechanical support structure for ELIADE has to be highly versatile to allow for the rearrangement of the setup according to the specific experimental needs and for the movement of the whole setup in different locations in the **E2** and **E8** experimental areas.

The mounting of the detectors will allow for a continuous modification of the detector-to-target distance from a minimum of 15 cm to a maximum of 30 cm.

The angle of the detectors placed around 90° can be varied between the nominal 90° and 100° . This is particularly useful in the case when the gamma beam scattering at forward angles close to 90° will produce a large background in the detectors and their shift towards backwards angles can improve the situation.

The central support was fitted with the possibility to rotate around the beam axis. This feature was implemented for two reasons:

- a 45° rotation will permit to place the CLOVER detectors or the $LaBr_3(Ce)$ detectors at the angles relevant for the polarization measurement without the need to dismount them;
- the rotation of the support will allow for the mounting of the detectors placed in vertical direction low position and in horizontal direction towards the electron accelerator where the available space is extremely reduced.

A 3D view of the mechanical support structure is shown in Fig.20. The central support and the backward one are separated and they can be moved apart over a distance of about 1 m. This is needed in case of replacing detectors on the array or when the central support has to be rotated.

The structures will be mounted on wheels that will allow for the positioning of the array in beam and its removal and parking when not used.

A support platform common to all the experiments will allow for a fast centering of the setup with millimeter accuracy on the beam axis. The accurate submillimeter alignment of the target on the beam axis will done by moving the tube holding the target and by using a high spatial resolution CCD camera attached to the tube. A detail of the target mechanical support is shown in Fig.21.

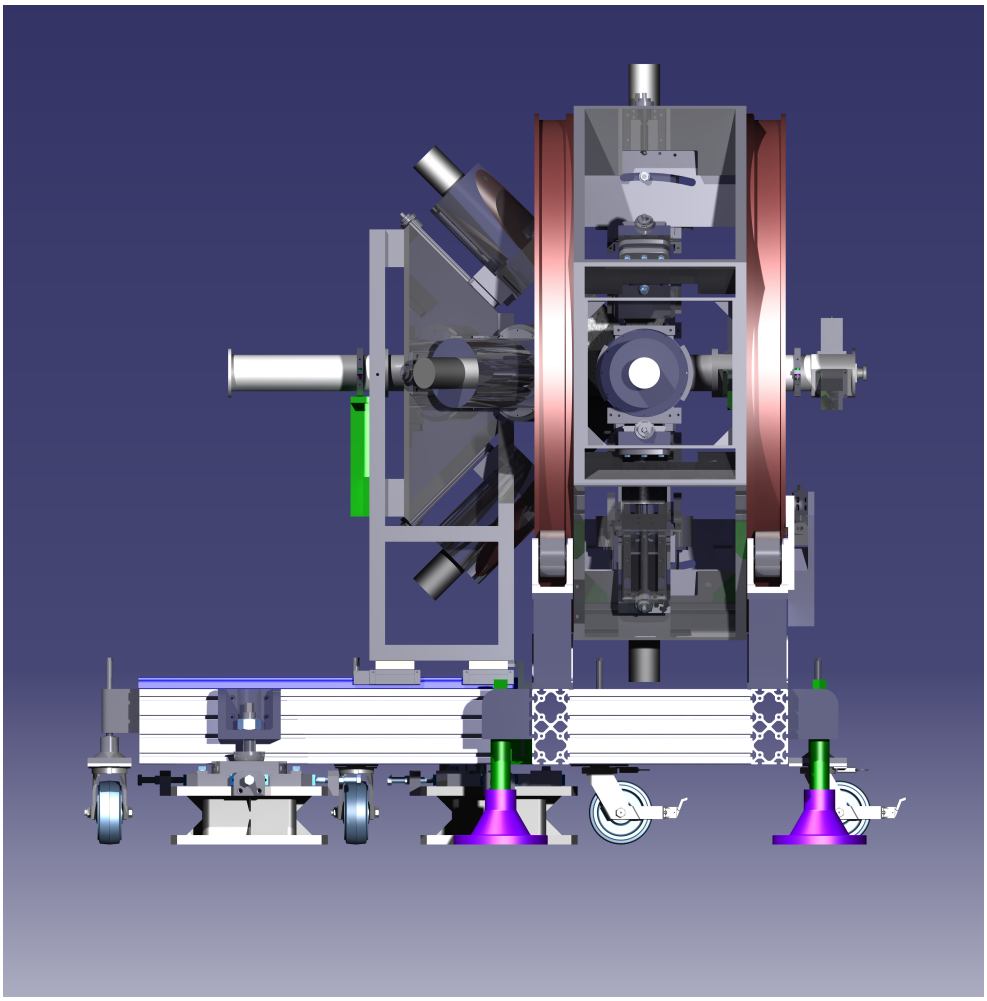

Figure 20 – Three-dimensional CAD of the ELIADE array. The two structures (for the detectors at 90° and for the detectors at 135°) can be separated over a distance up to 1 m.

The mechanical support structure will also act as support for the liquid nitrogen filling system distribution pipes and for the cable trays.

3.2.7. Alignment and Target systems

The alignment system is composed of three main sub-systems. The first one consists of a laser tracker system used during the mounting of the different components of the NRF experimental set-up and their alignment with respect to the Network of Reference Points of the building. The second sub-system is used for a pre-alignment of the mechanical structure with the beam axis and will be based on the

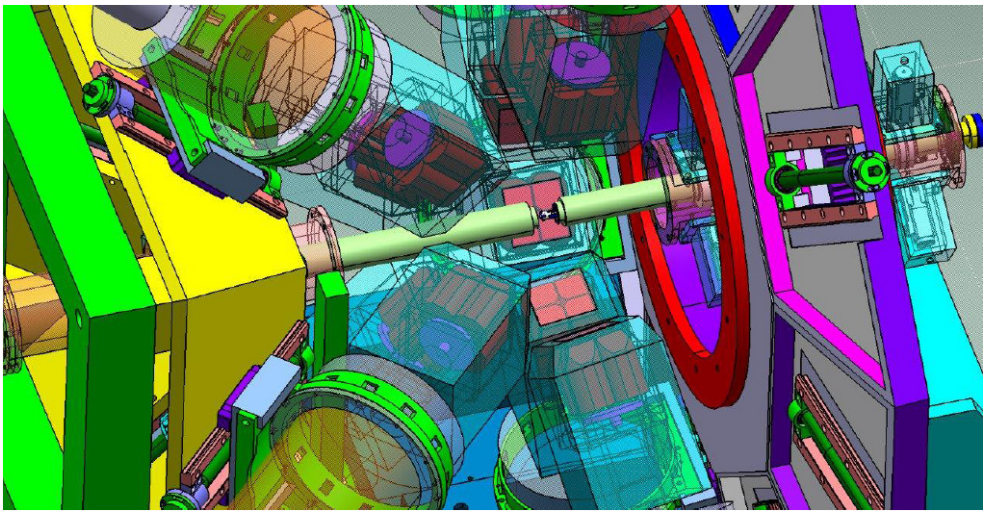

Figure 21 – Detail of the target holder and target centering system. The target is centered within a tube that can be aligned with the beam under vacuum with the use of a beam imaging system attached to the tube.

use of a laser pointer mounted on the gamma beam delivery system. A CCD system, also referred as beam imaging system, allows a sub-mm alignment of the mechanical structure with the beam. A detailed description of this system is available in the Gamma Beam Delivery and Diagnostics TDR [66].

The target mounting and alignment system is used in combination with the beam imaging system.

The target holding system is mounted inside the ELIADE Interaction Chamber (IC) and its alignment with the beam is possible due to two actuators allowing for a relative movement of the holding system against the IC. The target holder is referred as COLLIMATOR PIPE. Two collimators mounted at the two ends of the COLLIMATOR PIPE will be used for the alignment of the pipe and consequently of the target.

The movement of the COLLIMATOR PIPE will be performed by motors and the requirements for the control system are the following:

- Remote control of the position (OPEN/CLOSE) of the two collimators (stepper motors are proposed)
- Remote control of the motors that performs the movement of the COLLIMATOR PIPE, via a HMI located in the User Room.

The target holder will be inserted inside the COLLIMATOR PIPE such to ensure that the target is centered inside the pipe. The target will be automatically

aligned with the COLLIMATOR PIPE.

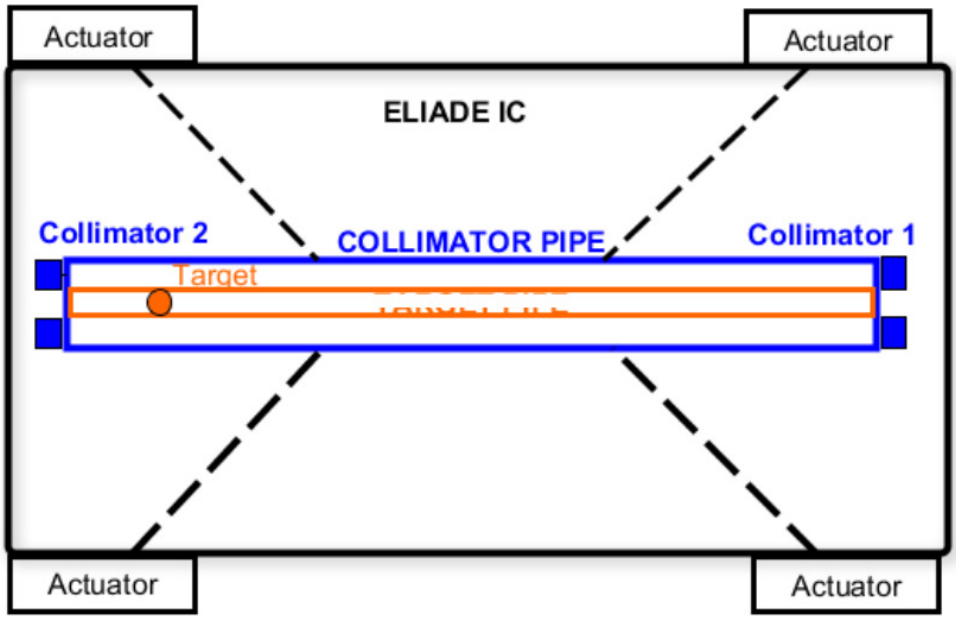

Figure 22 – Detail of the target holder and centering system. The target is centered within a tube that can be aligned with the beam under vacuum with the use of a beam imaging system

3.2.8. HV and LV power supplies

The ELIADE array will consist 8 segmented CLOVER detectors with 4 CsI(Tl) elements back-catcher anti-Compton shields and 4 $LaBr_3$(Ce) scintillator detectors. Optionally a 4 elements BGO rear side shielding can also be mounted around the CLOVER detectors. The elements of the CsI(Tl) back-catcher and of the BGO rear side shielding will be powered individually to allow for a good gain match of the different elements. The total number of High Voltage (HV) channels is 100.

A particular care has to be payed when applying/removing the HV on the Ge detectors. The HV has to be ramped up/down slowly while monitoring the reverse current on the Ge crystal. The high voltage can be applied on the Ge crystals only when they are cooled down to the liquid nitrogen temperature. Given the high number of channels the HV supply to all the detectors will be computer controlled. A dedicated program will perform the following tasks:

- application/removal of HV, monitoring the detectors status, enabling/disabling of the detectors

- data acquisition system, saving/restoring the detector specific parameters in/from databases,
- emergency actions from remote. The program will be controlled through a graphical user interface.

The control system will have to issue alarms and automatically execute actions corresponding to specific alarms. The HV control system will get information on the Ge crystals temperature from the liquid nitrogen filling system.

A multichannel HV power supply system able to host different HV boards specific for the different types of detectors used in the array is proposed. In the case of the Ge HV channels the system will accept individual trip signals that will shutdown the voltage on the detector with a predefined ramp down. Such trip signals are issued by the Ge detectors or the filling system when the temperature of the crystals is increasing accidentally.

The HV system will be placed under UPS to avoid accidental removal of the HV on the Ge detectors due to power failure. Even so, in case of accidental shutdown of the HV due to power failure, the power supply is provided with a protection system to block the instantaneous application of the full voltage when the power is restored.

All the detector signals will be read-out by preamplifiers. To ensure the operation of the preamplifiers they have to be powered with low voltage. For this purpose a low-voltage (LV) low-noise power supply delivering +6 V, -6 V, +12 V and -12 V will be provided. Given the large number of channels to be provided it is more efficient to acquire dedicated LV power supplies.

3.3. DIGITAL SAMPLING DATA ACQUISITION SYSTEMS

A digital readout system able to cope with signals from Ge crystals and BGO, CsI(Ta) and $LaBr_3$(Ce) scintillator crystals has to be developed. The proposed solution is based on the used of digital sampling electronics.

For the signals from Ge, BGO and CsI(Tl) a sampling rate of 250 Msamples/s and an accuracy of 14 bit are proposed. For the fast scintillator detectors $LaBr_3$ the signals will be sampled at 500 Msamples/s with an accuracy of 12 bit.

The proposed EDAQ scheme for ELIADE (Fig.23) is based on the idea that part of the data filtering (energy, time) will be performed inside the digitizer boards and one has to save only a short part of the signal pulse corresponding to the leading edge for further pulse shape analysis. The data rate estimates are made considering that the system is triggered at 100 Hz with the RF signal from the accelerator and one saves 1 μs of the signal pulse on disk. A 1 μs of the signal pulse will contain the leading edge of Ge detectors signals and also the full train of micropulses from the gamma beam. Local processing implies also zero suppression and a further reduction of the data set can occur.

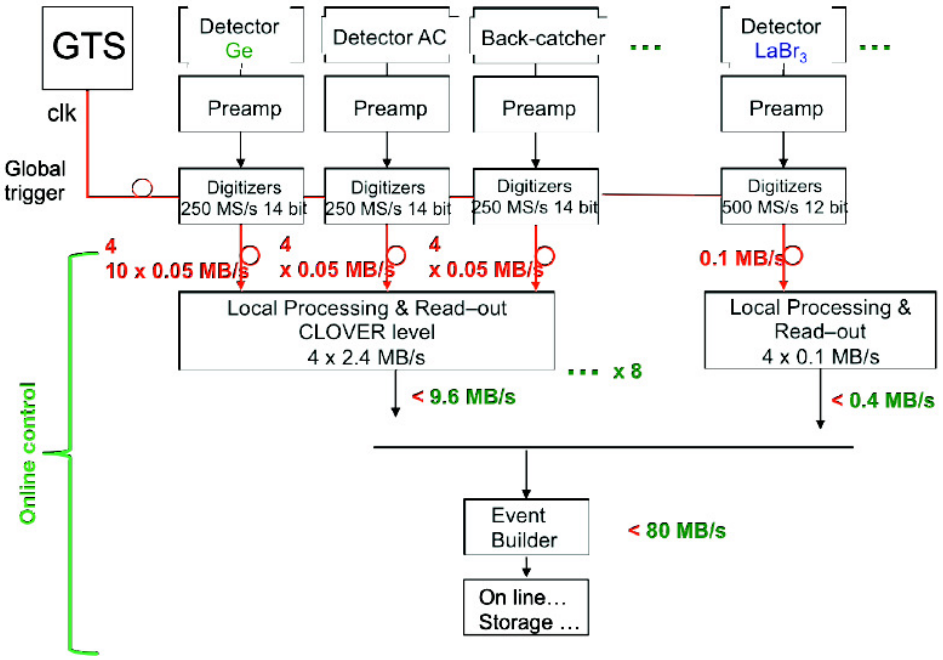

Figure 23 – Schematic layout of the digital data acquisition system for ELIADE. The signals from the Ge, anti-Compton shields and LaBr3 detectors will be digitally sampled.

The digital data from one segmented CLOVER will be sent to one Local Processing PC with enough data storage space and processing power. There will be 8 rack-mounted PCs for the CLOVER detectors, one for the $LaBr_3$(Ce) detectors and one for event building and online analysis.

The storage system should allow for long-term archiving of the experiment data and retrieval for data analysis.

The data acquisition system will consist of:

1. a set of commercial modular high density digitizers, to cover a total number of 388 spectroscopic channels including pulse shape analysis and pulse height analysis software;

2. correspondingly modular crates and related power supplies;

3. crate controllers with global synchronous clock and global trigger and sustained throughput rate to a main computer (requested mean value of about $\approx$ 200 MByte/s).

The solution is based on commercially available digital sampling modules. Flexibility in changing the digital algorithms, speed of data transfer, reliable syn-

chronization of different modules are criteria on which the final selection of the manufacturer will be done.

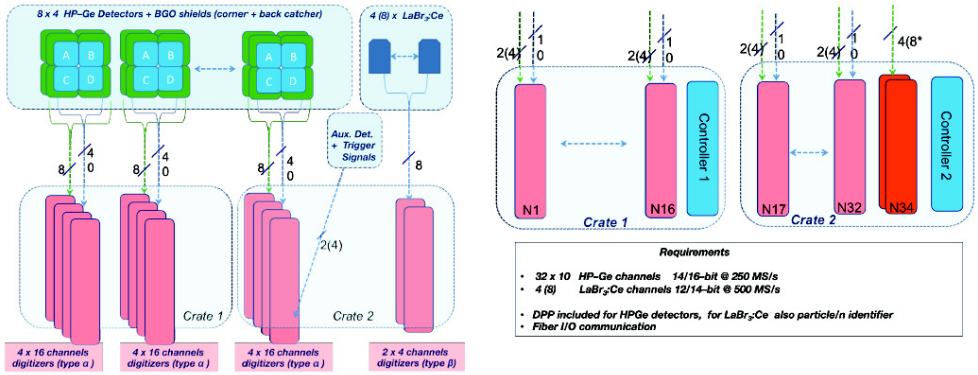

Figure 24 – Block-diagram of the ELIADE DAQ in the case of two crates with synchronized global clock distribution and global trigger.

The use of a synchronous global clock for all module is an important issue. Firstly, to get the sum peak out of active segments but also because the full energy peak can be obtained also by summing (add-back mode) the energies deposited in the adjacent detectors and in this case the corresponding digitizers could be placed even in different crates. Moreover, the global synchronous clock is needed also for the fast coincidence with auxiliary detectors and/or with beam detectors etc.

Two type of digitizers are considered: type α - for the HPGe detectors - with 14 bit resolution @ 250 MS/s (optionally 16 bit resolution @ 250 MS/s) and type β - for the $LaBr_3$(Ce) detectors or similar - with 12 bit resolution @ 500 MS/s (optionally 14 bit resolution @ 500 MS/s). The architecture of the FEE of the DAQ is shown in Fig. 24. If the selected digitizers will be manufactured with 16 channels /module the foreseen DAQ will consist of 32 modules type α and one module type β distributed in only two crates. Each crate is controlled by a crate-controller. The digitizers have to be synchronized with the same global clock, distributed to all digitizers; more over the digitizers acquisition mode has to be booted and started simultaneously.

The digitizers for HPGe detectors (type α) will have most probable a density of 16 channels/module. The two core input signals will be used as main triggers and all 8 segment input signals will be triggered with the OR function of the two core triggers. The anticoincidence of this signal with the OR signal of the three delayed BGO triggers is used to validate the core input signals, in an anti-Compton suppression set-up. The requested programmable delay width is in the range of 100 - 1000 ns.

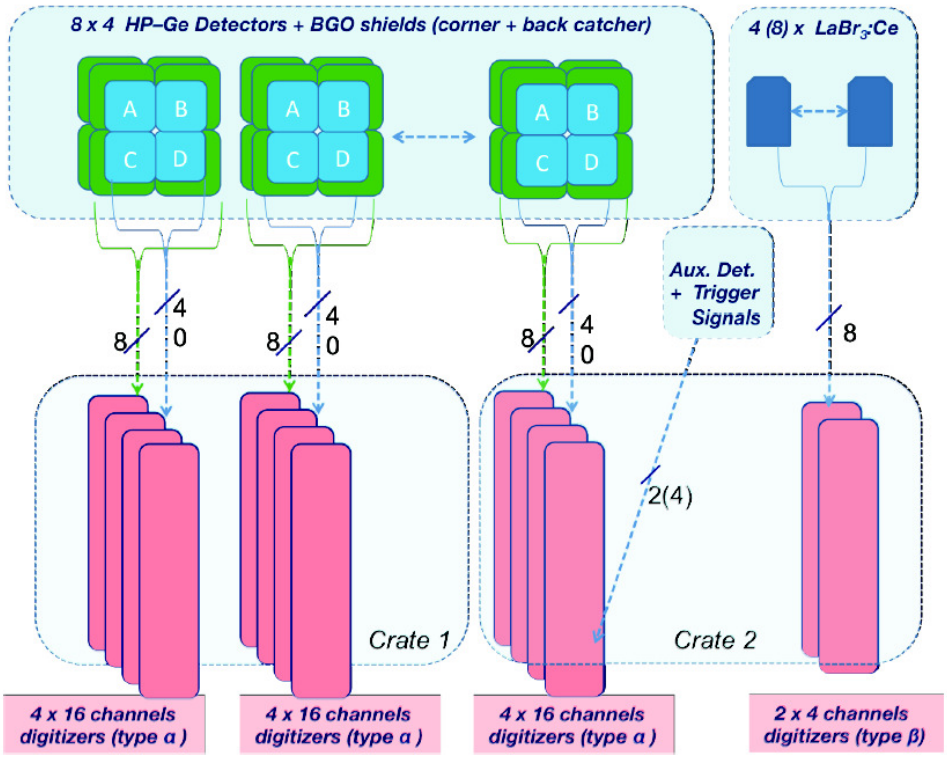

Figure 25 – The requested structure and main specifications for a 16 channels digitizer for HPGe detectors.

The main requested specifications of modular digitizers (type α) are summarized in Fig. 25: requested resolution 14 bits@250 MS/s; analog inputs: single ended 50 Ohm but, optionally, differential input signals while a development is foreseen to implement differential output signals in the FEE of HPGe detector assemblies, in a joined development with the manufacturer of the HPGe detectors.

The second type of digitizers (type β) dedicated for faster detectors (e.g. $LaBr_3$(Ce) or similar) has to have 500 MS/s and 12 bit resolution and 4 (or 8) channels per module. Each individual channel will be triggered independently.

3.4. LIQUID NITROGEN FILLING SYSTEM

The gamma-ray detector array is based on the use of HPGe detectors. For a proper operation of the Ge crystals they have to be cooled down to the temperature of liquid nitrogen (LN_2). For this reason Ge crystals are mounted in vacuum tight cryostats cooled with LN_2 supplied by an attached dewar. The dewars have to be

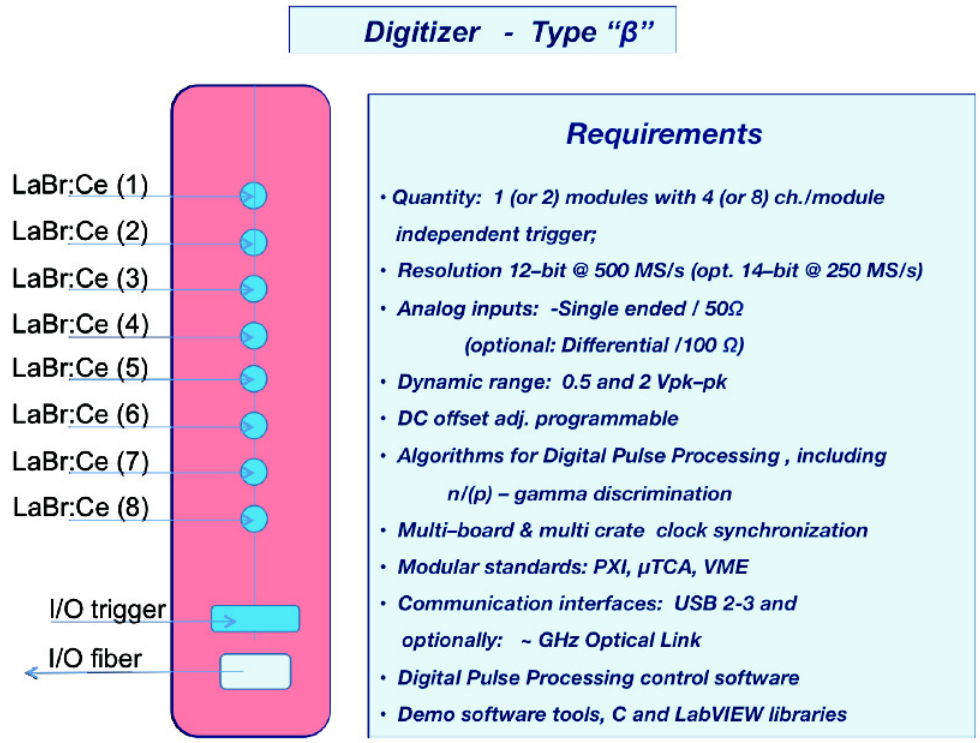

Figure 26 – The requested structure and main specifications for a digitizer for $LaBr_3$(Ce) detectors.

periodically (once or twice per day) filled with LN_2. The liquid nitrogen is taken from a 300 liters buffer tank located close to the experimental setup. The buffer tank will be filled once per day from the external 2000 liters liquid nitrogen tank.

3.4.1. LN_2 transfer lines

The transfer of the liquid nitrogen from the external tank to the internal buffer tank and from the buffer tank to the collectors will be done through transfer lines under vacuum. The liquid nitrogen will be distributed to the Ge detectors through a collector tube supplied with cryogenic valves.

The thermal insulation of the transfer line has to be of high quality to avoid large LN_2 consumption through vaporization when cooling down the line. The transfer line is made of isolated stainless steel tubes. The tubes have two chambers with vacuum in between them. The internal tube through which the LN_2 is flowing is wrapped in super-isolating material. The transfer line is made of several tube stubs interconnected with bellows to allow for the compensation of thermal expansion. The connection between the different tube stubs requires a careful work to ensure the in-

tegrity of the thermal insulation. Every tube stub is provided with a vacuum valve. Due to the complexity of the construction and installation of the LN_2 transfer lines the work has to be performed by experts qualified in the construction of cryogenic infrastructures.

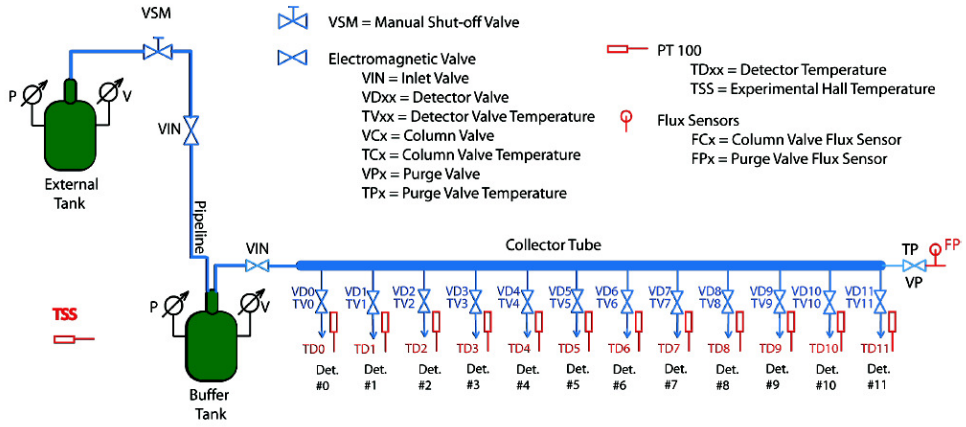

Figure 27 – Schematic layout of the LN_2 filling system for the ELIADE detector array.

For safety reasons automatic valves have to be mounted at the exit of the external and the internal buffer tanks. These valves will allow for the opening or closing of the LN_2 flux into the transfer line at the beginning and the end of the filling cycle. They will prevent the accidental opening of the valves outside the filling cycles and the dispersion of the LN_2 in the experimental vault.

The last part of the filling system consists of a collector tube with cryogenic electrovalves. There will be 12 valves for the Ge detectors and one purge valve. The purge valve is opened at the beginning of the filling procedure to let the liquid nitrogen to flow into the transfer system; it ensures that the collector is completely full with liquid nitrogen before the individual detector valves are opened. This way one avoids sending nitrogen gas at higher temperature into the detectors and warm them up. After the end of the filling cycle the purge valve is also used to exhaust the nitrogen gas from the transfer lines and lower the pressure in the line.

A schematic view of the LN_2 filling system for the ELIADE array is given in Fig. 27.

3.4.2. Autofill control system

The automated control of the LN_2 filling system has to keep the Ge detectors at the temperature of the liquid nitrogen without any external action. The system should allow for the monitoring of some critical parameters, allow users to make a minimum

set of operations and give the administrator access to the complete configuration of the system.

The control program should be implemented entirely in a hardware operating independently of the computer running the graphical user interface. In case of a power failure the system should restart automatically with the last saved configuration. A solution is the use of the control systems based on Compact Rio architecture from National Instruments. The detectors will be filled periodically at fixed intervals of time or when a request arrives from a detector (in case of warm up) or when the user ask for such an operation.

The control program has three phases of operation: monitoring, filling and post-filling. The program should make a data logging of parameters, messages and configuration. For a more reliable operation it should be integrated with the HV control system and the detector database. In case of failures and errors the system should issue critical alarms and dispatch them to the persons in charge through communication lines.

3.5. EXPERIMENTAL SETUP FOR SELF-ABSORPTION MEASUREMENTS

Self-absorption experiments are based on the comparison of beam intensities in measurements with and without absorber target in the beam line. Thus, a self-absorption measurement generally consists of two individual NRF measurements - a classic one and one with absorber target positioned in the beam line.

For both measurements the standard ELI-NP detector array can be used without any changes.

For the second measurement an absorber target made of the same material as the scatterer target (which is located in center of the detector array) has to be placed somewhere in the gamma beam such that the beam has to pass the absorber before reaching the actual target of interest. The detector array has to be properly shielded against photons scattered in the absorber target since those events would distort the actual self-absorption effect. Thus, the absorber target may, e.g., be placed inside the absorber as indicated in Fig.28

3.6. VACUUM CONTROL

The ELIADE array will have an interaction chamber (IC) under vacuum. The specifications are:

- the nominal vacuum level is better than 10^{-3} mbar;
- the vacuum inside the IC will be performed by several type of pump units;
- vacuum gauges (VG) will be used to monitor the value of the pressure inside the ELIADE IC;

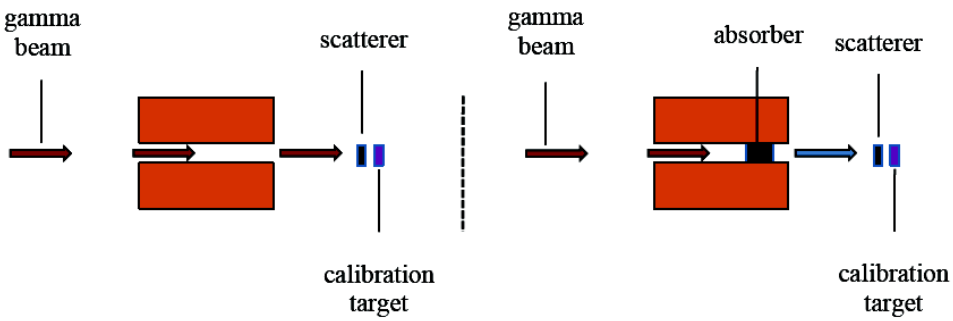

Figure 28 – Illustration of the self-absorption method experimental setup.

- the interface between the Gamma Beam Delivery low energy section pipe and the IC is only air.

In terms of control the requirements are:

- a remote monitoring of ELIADE IC vacuum in the User Room through a graphical user interface;
- a hardware interface shall provide the effective value of the ELIADE IC vacuum to the PLC Control system of the Gamma Beam Delivery (see TDR GBDD, Vacuum).

4. ESTIMATE OF COUNT RATES/FEASIBILITY OF PROPOSED DEVICES FOR SELECTED EXPERIMENTS

4.1. REMARKS ON THE BEAM PARAMETERS USED IN THE COUNT RATE ESTIMATES

The beam parameters used to estimate the count rates for some of the proposed experiments are based on the values published on the ELI-NP web page http://www.eli-np.ro/documents/ELI-NP-GBS-Specifications- rev3-1.pdf and in Ref. [68]. The first document gives a summary of the beam parameters over the whole range of photon energies while the second one gives more details for four different available energies. The reported values correspond to a distance of 10 m from the interaction point.

In determining the beam parameters relevant for the feasibility of the experiments one has to consider that the NRF setup will be located at a distance of about 15 m from the interaction point (immediately after the EuroGammaS gamma beam diagnostics setup).

Given that we are interested in using small quantities of rare or enriched target materials the estimates are made considering the gamma photon spectral density

corresponding to a surface of 1 mm^2. An estimate of this value can be obtained directly from the table reported in Ref. [68]: at photon energies between 2 and 3 MeV the spectral density is between 4×10^4 and 2×10^4 photons/s/eV with a divergence between 140 μrad and 100 μrad, respectively. At a distance of 15 m these values translate to a beam spot of 1.5-2 mm radius, leading to a flux of about 5×10^3 photons/s/eV/mm^2.

4.2. CONSTRAINTS ON $0\nu\beta\beta$-DECAY MATRIX ELEMENTS FROM A NOVEL DECAY CHANNEL OF THE SCISSORS MODE OF ^{150}SM

The integrated cross sections of $J^\pi = 1^+$ scissors mode states of ^{150}Sm are in the order of $I_{s,0} = 8 - 43eV \cdot b$. The well-known count rates are:

$$R_{i,f} = \Phi_\gamma(E_i) N_T I_{s,f} \epsilon(E_\gamma) W(\theta, \phi)$$

Here, $\Phi_\gamma = 5 \cdot 10^3$ gammas/(eV$\cdot$ s $\cdot$ mm^2) is the photon flux, N_T the number of target nuclei, ϵ the photo-peak efficiency, and $W(\theta, \phi)$ the angular correlation. For a target mass of 50 mg/mm^2 this correspond to an excitation rate of the scissors mode states of 800-4300 per second.

A 1% branch to the 0_2^+states with a photo-peak efficiency of 3% at 2.3 MeV results in a count rate $R_{1^+ \to 0_2^+} = 0.24 - 1.3$ counts/s. However, the observation of such a decay branch would largely benefit from a coincident detection of the de-exciting γ's of the 0_2^+ state which reduces the background significantly.

4.3. ROTATIONAL 2^+ STATES OF THE NUCLEAR SCISSORS MODE

The ELI-NP γ-ray setup will reach a population of such a 2^+ state of about 0.1/s for a deformed A $\approx$ 150 nucleus and 0.2 g/cm^2 target mass.

4.4. LOW-ENERGY DIPOLE RESPONSE OF NUCLEI IN THE ACTINIDES REGION

4.4.1. Example I: ^{240}Pu

Estimate of background from α decays:

Assumption: 10 mg (=2.5x10^{19} nuclei) enriched ^{240}Pu, partly contaminated with ^{239}Pu.

From $T_{1/2} = 2 \times 10^1$1s one expects 6×10^7 decays/s to the daughter nucleus ^{236}U ($T_{1/2} = 2 \times 10^7$y). A fraction of 73% of these decays go to the ground-state and 27% to the 45 keV excited state. In addition one has to expect X-rays around 100 keV. Assuming 1 gamma per decay, a Ge(HP) (1% total efficiency) would see about 500 kHz of gammas, however, due to the low energy these can be easily reduced to a negligible rate by a Pb filter (interesting lines in ^{240}Pu are expected at above 500

keV). The same arguments hold true for ^{239}Pu; here the α decay goes with 70% to a 8 keV state and with 17% to a 13 keV state in the daughter nucleus.

In summary, the background problems with a 10-100 mg ^{240}Pu target should be solved with adequate filters in front of the detectors.

Estimate of reaction rates from the target:
Assumption: an $E1$ excitation at 500 keV with Γ_0=50 meV (these are values taken fom ^{238}U); a $M1$ excitation at 2000 keV with Γ_0=25 meV. Γ_0/Γ = 12; beam intensity 5000 gammas/(eV·mm$^2 \cdot s$); 10 mg ^{240}Pu target in pencil like configuration 1mm ^{2} diameter.

First estimate: 50-200 reactions/s. This means about 1 good reaction/s in the Ge detector.

4.4.2. Example II: ^{248}Cm

Estimate of background from α decays: the background from natural radioactivity of the target material (and contaminants) is often a limiting factor. In our case from a 10 mg (=2.4 x 10^{19} nuclei) enriched ^{248}Cm ($T_{1/2} = 1.09 \times 10^{13}$ s) one expects 1.6×10^6 decays/s to the daughter nucleus ^{244}Pu ($T_{1/2} = 8 \times 10^7$ a). About 75% of these decays go to the ground state, and 16.5% to the first 2^+ state at 44.2 keV. In addition one has to expect X-rays around 100 keV. Assuming one X-ray per decay a HPGe detector (with 0.6% total efficiency) would see about 10 kHz of gammas. However, due to the rather low energy these can be easily reduced to a negligible rate by adequate filters in front of the detectors (the γ transitions of interest in ^{248}Cm are expected above 500 keV). In summary, the background problems with a 10 - 100 mg ^{248}Cm target should be solvable.

Estimate of reaction rates from the target: for the rate estimate we assume a dipole transition with a gamma-ray transition energy of 1000 keV and an integrated cross section of around 30 eV·b (value taken fom the neighboring nucleus ^{240} Pu). The photon flux from ELI-NP is assumed to be about 5000 photons per eV·s·mm^2. If one would use the planned ELIADE array of eight detectors with a total photopeak efficiency of 5% at 1.3 MeV, this would yield 8000 cts/h in the single (non-coincident) HPGe detector spectra from a 10 mg enriched target of ^{248}Cm.

4.5. DIPOLE RESPONSE AND PARITY MEASUREMENTS FOR WEAKLY-BOUND NUCLEI

In order to estimate the expected count rates and the target material that is needed to perform these experiments at ELI-NP, 10% of the known ground-state decay width (280 meV) of the two-phonon state in the neighboring nucleus ^{140}Ce is taken as a reference value. With a natural composed cerium powder target of 0.05 mg mass, an estimated ground-state decay width of 28 meV, an absolute photopeak efficiency of the HPGe array of 5% (8 detectors) and a photon flux of 5000 photons

per eV·s·mm^2, single detector count rates of 200 counts/h and 2000 counts/h could be achieved in the single HPGe spectra. This would allow for the study of these 1^- states, including spin, parity, and $B(E1)$ strengths measurements.

4.6. SELF-ABSORPTION MEASUREMENTS AT ELI-NP

Using a scatterer target of 1g of ^{140}Ce and an absorber target of 10g of ^{140}Ce (a rather thick absorber is - independent from the photon flux - needed to get a significant self-absorption) the small branching ratio of an excited state with, e.g., γ 0 =50meV and γ=500meV (Γ_0/Γ=10%) in the PDR region ($\approx$ 6MeV excitation energy) to the ground state could be measured within 2h to an accuracy of 5%. Assuming at a bandwidth of 1% the entire PDR region in ^{140}Ce could be investigated within 2 days offering new insight to the PDRs decay pattern.

5. SPECIFIC NEEDS AND UTILITIES, TRANSVERSAL NEEDS

5.1. INFRASTRUCTURE NEEDED FROM ELI-NP

1. Clean power supply lines; clean grounding connections; UPS

   UPS units are necessary in case of either short or long power shutdowns. The aim is to keep the system running for very short (ms) shutdowns. For longer shutdowns, the aim is to deliver power long enough to shutdown properly the environment slow control, vital electronics and to finalize a possible LN2 filling. Therefore, the time autonomy of the UPS units will be limited to about 15 min. and their power capacity overestimated. On detection of power failure by the UPS a shutdown procedure should be defined on how to shutdown non-vital system. Any system connected to the UPS is desirable that it may be shutdown remotely to allow power to be used for more critical subsystems on the same UPS.

2. Mechanical

   Mounting, dismounting the detectors from the array and the transport from one experimental point to another will need to be performed in coordination with the available space and the other activities being performed at the same time.

3. Vacuum

   The target of the array will be placed in vacuum, so a connection for the control of the vacuum on the corresponding section of the beam transport line will have to be established.

4. Liquid Nitrogen

   The detector array uses liquid nitrogen. The dewars used for the liquid nitrogen system (a 2000 l storage tank outside the building and 300 l next to the detectors) are provided, filled and maintained by ELI-NP services.

5.2. COMMON INFRASTRUCTURE WITH OTHER EXPERIMENTAL SETUPS

1. Mechanical mounting and alignment devices
2. Cable ducts
3. Network connection
4. Data storage and computing power

5.3. GAMMA BEAM POLARIZATION SWITCHING DEVICE

Parity measurements in NRF experiments require polarization information on one of the γ quanta involved. Either a polarized γ beam must be used in the entrance channel or polarization must be measured in the exit channel. Measuring the polarization of scattered photons using Compton polarimeters has been very successful at energies near and below 3 MeV. However, this technique becomes difficult at excitation energies exceeding 4 MeV because the analyzing power of the Compton scattering process is energy dependent and approaches zero at these energies. The use of polarized photons in the entrance channel and the measurement of the intensity distribution with respect to the polarization plane of the beam is preferable for parity measurements of nuclear dipole excitations above about 4 MeV: the analyzing power of this process is 100% and independent of the scattered γ-ray energy [16]. Moreover, parity information can be obtained from relatively simple intensity measurements (see Section 1.2). For this kind of measurements **linear polarization** of the gamma beam is needed.

Linear polarization switching and circular polarization of the gamma beam allow for the minimization of the systematic errors of the measured data and lead to a sizable increase in the sensitivity of the measurements.

On the fundamental topics, NRF with high-resolution **circularly polarized** gamma beam of ELI-NP will provide a sensitive method to measure the parity non-conservation of nucleon-nucleon interaction [69]. The high-energy parity doublets in light nuclei such as ^{14}C, ^{14}N, ^{15}O, ^{16}O, ^{18}F and ^{20}Ne (see Section 2.2) are suggested as best cases for study because the $E1/M1$ and $E2/M2$ mixing is expected to be enhanced due to small energy difference in between the doublet members.

6. SAFETY REQUIREMENTS

6.1. GENERAL SAFETY

The safety of the persons working in the ELI-NP facility will be handle by the ELI Personal Safety System (ELI-PSS). The scope of ELI-PSS is:

- access control in the areas where a risk exists (this supposes that all the risks have been evaluated);
- monitoring and alarm of the radiations level in the facility areas;
- respect of safety procedures related to the use of dedicated components/systems for the experiment (LN_2 , High Voltage, Vacuum, etc.)

Are not in the scope of ELI-PSS:

- general safety risks such as fire safety (Detection & Extinction), CO_2 & O_2 monitor, temperature, etc; these risks are controlled by different systems composing the Building Management System (BMS) and could be interfaced with the ELI-PSS; the Door Interlock and the Control Access systems are also in the scope of the BMS; however, these will be directly integrated within the ELI-PSS.
- the physical protection such as shields, clothes and glasses that shall be worn, etc.

To summarize, the ELI-PSS have to handle all the risks induced directly by the different phases of all the experiments (set-up, start, run, and maintenance).

The ELI-PSS will master several safety sub-systems distributed in the facility. All the safety sub-systems should work independently and be able to take a decision (open a mechanic contact, activate a shutter, etc.) whenever it is needed. In the case of the NRF experiments these subsystems are:

- GBS Safety System: the GBS Safety system will handle the access control to the GBS machine areas and implement a radiation alarm system in these areas [68];
- Experimental PSS that should cover all the risks that could happened during the different phases of one experiment (calibration, set-up, run, maintenance).
- The BMS Door Interlock
- The Radiation Monitoring System that shall monitor the radiations level in the entire facility, along with alarms, flash lamps, etc.

The sc hematic layout shown in Fig. 29 summarizes these ideas.

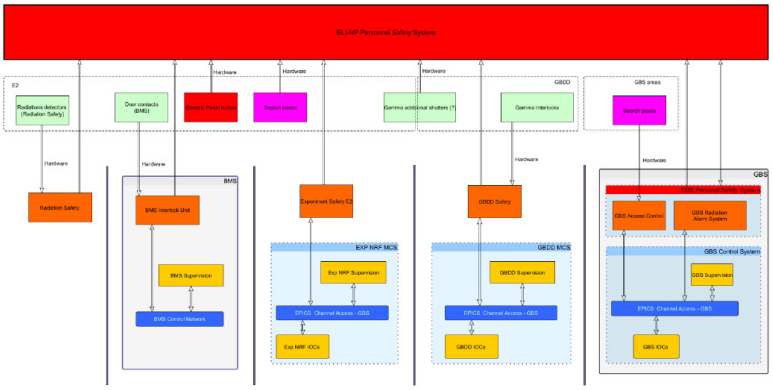

Figure 29 – Schematic layout of the ELI-NP Personnel Safety System and the interconnection with the NRF and GBDD systems.

6.2. ACCESS TO THE EXPERIMENTAL AREA

This section deals with the presence of the Users in the experimental area. An **Access Safety Procedure** shall be followed to ensured that:

- The level of radiations in E2 and E8 areas has to be under the threshold given by the radiation safety sub-system;
- The access to the E2 or E8 area is impossible if the accelerator is ON;
- To access E2 or E8, the User shall use the Door Interlock system based on the key panels and shall also have the rights (code & card) to enter in this area;
- The presence of one person in E2 or E8 shall be continuously indicated to the ELI-PSS.

A Safety Start Experiment request should be followed each time a User ask for running an experiment using the Gamma Beam.

1. Safety Configuration request
   (a) The configuration of the experiment is registered via the EPICS Control System: the beam parameters (energy, time structure, etc.) requested, the experimental area (E2, E7, and E8), and the vacuum level inside the ELIADE reaction chamber;
   (b) This configuration is sent to the Accelerator Operator and to the ELI-PSS;
   (c) The Accelerator Operator configures the GBS via the EPICS based Gamma Control System. The configuration is sent to the ELI-PSS;

(d) The ELI-PSS compares two SW inputs related to the beam parameters (User and Operator) that it received. If the two inputs are the same, an OK signal is delivered, the procedure continues, go to 2. If not, the procedure restart, go to 1.

2. Safety Experiment request

(a) Once the set-up of the experiment is completed, the ELI-PSS shall collect interlocks signals coming from GBS, GBDD and the E2/E8 area (BMS Interlock signals, Radiations Interlocks signals, ELIADE reaction chamber interlock signals);

(b) The ELI-PSS will generate a truth table that will be compared with the ”Safety truth table” that has to be implemented and upgraded for each experiment;

(c) If the outputs of the truth tables do not match the outputs of the ”Safety truth table”, an interruption of the Safety Start Procedure is generated and send to the Experiment Safety, and GBS Safety. The Procedure restarts, go to 2. If the outputs of the truth tables match the outputs of the ”Safety truth table”, an OK signal is delivered, go to 3.

3. Safety Clean Area request

(a) Accelerator Search Procedure: Warning lights must be flashing and audible warning must be given inside radiation areas before the accelerator is planned to be turned on. Before starting the accelerator a radiation area search must be initiated by the activation of a ”search start” button. ”Search confirmation” buttons mounted along the search path must also be provided. A ”Search complete” button at the exit point must also be set.

(b) If the Search Procedure is not complete, it should be restarted, go to 3a. If the Search Procedure is complete, go to 3c.

(c) Experimental Area Search: a similar procedure will be initiated for the experimental areas of interest (E2).

(d) If the Search Procedure is not complete, it should be restart, go to 3c. If the Search Procedure is complete. The system is ”safe” for the users but might not be for the machine.

7. CONTROL SYSTEM

The ELI-NP E2/E8 experimental areas will be partially dedicated to the Nuclear Resonance Fluorescence experiment. These areas will have the experiment

monitoring and control systems architecture similar to the GBS [68] and GBDD [66] control systems. The architecture is based on EPICS which will permit local distributed control of the equipment and additional clients to remotely supervise/control the experiment. This solution will allow a standardization of the control systems inside ELI-NP, while providing easy maintenance, better security, better logging and interfacing methods between the experimental areas, GBS and GBDD. A dedicated UserRoom will be used to remotely control from outside the E2/E8 areas the equipment as the experiment is running. An EPICS framework will be developed to link the experimental area to the UserRoom using a dedicated clientserver architecture that will allow maintenance and upgrades to be performed without interacting with other systems. A data storage server will be available for short term experimental data saving and this shall benefit in general from dedicated data busses, separated from the clientserver EPICS architecture that controls and monitors the equipment itself, in order to achieve the highest data throughput.

Dedicated EPICS servers are envisaged to interface the equipment necessary in the experiment such as:

- Target holding and alignment system composed of several motorized stages
- Beam imaging system including one CCD camera
- ELIADE detectors: interface between the LN_2 auto-filling & HV system and the EPICS framework to ensure the monitoring of the temperature and the high-voltage of the HPGe crystals
- Vacuum system for the ELIADE interaction chamber: interface between the vacuum system of the ELIADE interaction chambers and the EPICS framework
- DAQ system including time-stamping system

The equipment will have a Human Machine Interface able to locally (from inside the interaction area) or remotely (from the UserRoom) monitor and control the parameters needed to run the equipment and the experiment. For the equipment where the API is not provided, or the required development time does not fit into the general schedule, the link between the UserRoom and the experimental area, if needed, will be made using remote desktop (or similar) and by using the equipment proprietary software. The UserRoom will also provide through the EPICS architecture information to the user regarding the GBS parameters and GBDD configuration. The GBS and GBDD parameters will be controlled from the Gamma control room by the operators, from personnel and machine safety reasons.

8. COLLABORATIONS

- Memorandum of Understanding with Technische Universität Darmstadt, Germany
  - Physics case definition
  - Data Acquisition system definition
- Memorandum of Understanding with Institut für Kernphysik, University of Cologne
  - Physics case definition
  - Front–end electronics for Ge detectors
  - Ge detectors testing
- IFIN-HH
  - Detector development
  - EDAQ development
  - Test experiments

Acknowledgements. CAU, BB, MC, CM, CP, GS, EU were supported by the Project Extreme Light Infrastructure - Nuclear Physics (ELI-NP) - Phase I, a project co-financed by the Romanian Government and European Union through the European Regional Development Fund.

REFERENCES

1. R.R. Metzger, Prog. Nucl. Phys. 7, 54 (1959).
2. U.E.P. Berg and U. Kneissl, Ann. Rev. Nucl. Part. Sci. 37, 33 (1987).
3. U. Kneissl, H.H. Pitz, and A. Zilges, Prog. Part. Nucl. Phys. 37, 349 (1996).
4. U. Kneissl, N. Pietralla, and A. Zilges, J. Phys. (London) G32, R217 (2006).
5. K.S.Krane, R.M.Steffen and R.M. Wheeler, Nucl. Data Tab. 11, 351 (1973).
6. L.W. Fagg and S.S. Hanna, Rev. Mod. Phys. 31, 711 (1959).
7. P.B. Moon, Proc. Phys. Soc. A64, 76 (1951).
8. M. Goldhaber, L. Grodzins and A.W. Sunyar, Phys. Rev. 105, 1015 (1958).
9. R.L. Mossbauer, Zeit. Phys. 151, 124 (1958).
10. L.I. Schiff, Phys. Rev. 70, 761 (1946).
11. E. Hayward and E.G. Fuller, Phys. Rev.106, 991 (1957).
12. D. Bohle *et al.*, Phys. Lett. B137, 27 (1984).
13. F.D. Seward *et al.*, Phys. Rev. 121, 605 (1961).
14. J.S. O'Connell *et al.*, Phys. Rev. 126, 228 (1962).
15. H. Ohgaki *et al.*, Nucl. Instr. Meth. Phys. Res. A353, 384 (1994).
16. N. Pietralla *et al.*, Phys. Rev. Lett. 88, 012502 (2002).

17. N. Pietralla *et al.*, Nucl. Instr. Meth. Phys. Res. A483, 556 (2002).
18. N. Pietralla *et al.*, Nuclear Structure Physics with a Free Electron Laser, in Frontiers of Nuclear Structure 2002, P. Fallon and R. Clark Eds., AIP Conference Proceedings 656, American Institute of Physics, New York, 2003,pp. 365.
19. H.R. Weller, M.W. Ahmed, H. Gao, W. Tornow, Y.K. Wu, M. Gai, and R. Miskimen, Prog. Part. Nucl. Phys. 62, 257 (2009).
20. V.N. Litvinenko and J.M.J. Madey, Nucl. Instr. Meth. Phys. Res.A375, 580 (1996).
21. V.N. Litvinenko *et al.*, Nucl. Instr. Meth. Phys. Res.A407, 8 (1998).
22. B. Loher *et al.*, Nucl. Instr. Meth. Phys. Res.A723, 136 (2013).
23. N. Pietralla *et al.*, Phys. Rev. C65, 047305 (2002).
24. C. Fransen *et al.*, Phys. Rev. C 70, 044317 (2004).
25. D. Savran *et al.*, Phys. Rev. C 71, 034304 (2005).
26. T.C. Li *et al.*, Phys. Rev. C 73, 054306 (2006).
27. N. Pietralla *et al.*, Phys. Lett. B681, 134 (2009).
28. A.P. Tonchev *et al.*, Phys. Rev. Lett. 104, 072501 (2010).
29. D. Savran, T. Aumann and A. Zilges, Prog. Part. Nucl. Phys. 70, 210 (2013).
30. N. Tsoneva and H. Lenske, Phys. Rev. C 77, 024321 (2008).
31. E.G. Lanza *et al.*, Phys. Rev. C89, 041601(R) (2014).
32. S. Goriely, Phys. Lett. B436, 10 (1998).
33. V. Baran *et al.*, Phys. Rev. C88, 044610 (2013).
34. B.A. Brown and A. Schwenk, Phys. Rev. C89, 011307(R) (2014).
35. A. Krugmann *et al.*, Eur. Phys. J. Web Conf. 66, 02060 (2014).
36. T.D. Lee and C.N. Yang, Phys. Rev. 104, 254 (1956).
37. C.S. Wu *et al.*, Phys. Rev. 105, 1413 (1957).
38. E.G.Adelberger and W.C.Haxton, Ann. Rev. Nucl. Sci. 35, 501 (1985).
39. B. Desplanque *et al.*, Phys. Rev. C 77, 064002 (2008).
40. A.I. Titov *et al.*, J. Phys. G: Nucl. Part. Phys. 32, 1097 (2006).
41. J. Beller, N. Pietralla *et al.*, Physics Letters B 741, 128 (2014).
42. Y. Fukuda *et al.*, Phys. Rev. Lett. 81, 1562 (1998); A. Ahmed *et al.*, Phys. Rev. Lett. 89, 011302 (2002); K. Eguchi*et al.*, Phys. Rev. Lett. 90, 021802 (2003)
43. F.T. Avignone *et al.*, Rev. Mod. Phys. 80, 481 (2008).
44. J. Barea *et al.*, Phys. Rev. Lett. 109, 042501 (2012).
45. J. Beller *et al.*, Phys. Rev. Lett., in press.
46. J.F. Ziegler *et al.*, Nucl. Phys. A564, 366 (1993).
47. K. Heyde, P. von NeumannCosel, and A. Ricter, Rev. Mod. Phys. 82 (2010).
48. L.P. Gaffney *et al.*, Nature 497, 199 (2013).
49. M. Guttormsen *et al.*, Phy. Rev. Lett. 109, 162503 (2012).
50. B.J. Quiter *et al.*, Phys. Rev. C 86, 034307 (2012).
51. B.J. Quiter *et al.*, Lawrence Berkeley National Laboratory Paper LBNL5721E(2013).
52. M.S. Johnson *et al.*, Lawrence Livermore National Laboratory Paper LLNLTR483851 (2011).
53. G. Suliman *et al.*, Rom. Rep. Phys. 68, S799 (2016).
54. N. Pietralla *et al.*, Phys. Rev. C 51, 1021 (1995).
55. L.I. Schiff, Phys. Rev. 83, 252 (1951).
56. NNDC, http://www.nndc.bnl.gov
57. M. Scheck *et al.*, Phys. Rev. C 87, 051304(R) (2013).

58. C. Romig *et al.*, Phys. Rev. C 88, 044331 (2013).
59. J. Isaak *et al.*, Phys. Lett. B 727, 361 (2013).
60. S.L. Shepherd *et al.*, Nucl. Instr. Meth. Phys. Res. A434, 373 (1999).
61. C.W. Beausang *et al.*, Nucl. Instr. Meth. Phys. Res. A452, 431 (2000).
62. H.C. Scraggs *et al.*, Nucl. Instr. Meth. Phys. Res. A543, 431 (2005).
63. C.E. Svensson *et al.*, Nucl. Instr. Meth. Phys. Res. A540, 348 (2005).
64. L.–L. Andersson *et al.*, Nucl. Instr. Meth. Phys. Res. A622, 164 (2010).
65. S. Agostinelli *et al.*, Nucl. Instr. Meth. Phys. Res. A506, 250 (2003).
66. H.R. Weller *et al.*, Rom. Rep. Phys 68, S447 (2016).
67. C. Romig *et al.* Physics Letters B 744, 369, (2015).
68. O. Adriani *et al.*, Technical Design Report; EuroGammaS proposal for the ELI–NP Gamma beam System, arXiv:1407.3669v1 physics.acc-ph.
69. N.V. Zamfir *et al.*, Diode-Pumped High Energy and High Power Lasers; ELI: Ultrarelativistic Laser-Matter Interactions and Petawatt Photonics; and HiPER: the European Pathway to Laser Energy, edited by J. Hein, L. O. Silva, G. Korn, L. A. Gizzi, C. Edwards, Proc. of SPIE Vol. 8080, 80800X, 2011.